

# Strong Coupling Constant Determination from the new CTEQ-TEA Global QCD Analysis

Alim Ablat,<sup>1,\*</sup> Sayipjamal Dulat,<sup>2,3,†</sup> Marco Guzzi,<sup>4,‡</sup> Joey Huston,<sup>3,§</sup>  
Kirtimaan Mohan,<sup>3,¶</sup> Pavel Nadolsky,<sup>3,\*\*</sup> Dan Stump,<sup>3,††</sup> and C.-P. Yuan<sup>3,††</sup>

<sup>1</sup>*School of Physics and Electrical Engineering, Kashi University, Kashi, Xinjiang 844000 China*

<sup>2</sup>*School of Physics Science and Technology, Xinjiang University, Urumqi, Xinjiang 830046 China*

<sup>3</sup>*Department of Physics and Astronomy,*

*Michigan State University, East Lansing, MI 48824, USA*

<sup>4</sup>*Department of Physics, Kennesaw State University, Kennesaw, GA 30144, USA*

(Dated: January 1, 2026)

We present a new determination of the strong coupling constant  $\alpha_s$  from a global QCD analysis CT25 of parton distribution functions (PDFs) that incorporates high-precision experimental measurements from the Run-2 of the Large Hadron Collider together with a large sample of other measurements over a wide interval of energies. This work addresses two objectives: providing an up-to-date determination of  $\alpha_s$  using NNLO calculations and a sensitive nucleon data set within a self-consistent framework, and critically assessing the robustness of the  $\alpha_s(M_Z)$  extraction in light of systematic uncertainties as well as correlations of  $\alpha_s(M_Z)$  with the functional forms of PDFs and other model parameters. In regard to the uncertainty assessment, we demonstrate that some commonly used criteria, including the dynamical tolerance and Bayesian hierarchical models, may produce significantly different or even unstable estimates for the net  $\alpha_s$  uncertainty, and we introduce a concept of *data-clustering safety* that the replicable uncertainty estimates must satisfy. Based on this in-depth examination of the CT25 global hadronic data set using a combination of analysis methods, and after demonstrating a weak correlation between  $\alpha_s$  and the functional forms of CT25 PDF parametrizations, we find  $\alpha_s(M_Z) = 0.1183^{+0.0023}_{-0.0020}$  at the 68% credibility level.

---

\* [alimjanablat@outlook.com](mailto:alimjanablat@outlook.com)

† [sdulat@hotmail.com](mailto:sdulat@hotmail.com)

‡ [mguzzi@kennesaw.edu](mailto:mguzzi@kennesaw.edu) – Corresponding Author

§ [huston@msu.edu](mailto:huston@msu.edu)

¶ [kamohan@msu.edu](mailto:kamohan@msu.edu) – Corresponding Author

\*\* [nadolsky@msu.edu](mailto:nadolsky@msu.edu) – Corresponding Author

†† [stump@pa.msu.edu](mailto:stump@pa.msu.edu)

††† [yuanch@msu.edu](mailto:yuanch@msu.edu)

## CONTENTS

I. Introduction	3
II. Relevant aspects of the CT25 global analysis	6
II.1. Selection of data sets	6
II.2. The CTEQ-TEA goodness-of-fit function	9
II.3. Limitations of existing models for correlated systematics	11
III. Sources of uncertainties on QCD coupling	12
III.1. The PDF parametrization uncertainty is small...	12
III.2. ...but the systematic uncertainty remains	14
IV. Tolerances and data clustering safety	19
IV.1. Global and Dynamical Tolerance Criteria	20
IV.2. Properties of the dynamic tolerance	22
IV.3. Data clustering safety of uncertainty estimates	24
IV.4. Data reclustering and $K$ -folding	26
IV.4.1. Reclustering algorithm	26
IV.4.2. Separate reclustering of residuals and nuisance parameters	27
IV.4.3. $K$ -folding impact on $\alpha_s$	29
V. Bayesian Models for Uncertainty Estimation	33
V.1. Bayesian Hierarchical Model	33
V.2. Hierarchical Models via a Gaussian Mixture Model	34
V.3. Information Criteria and the GMM	36
VI. Final combination of $\alpha_s$ determinations	37
VI.1. The central $\alpha_s$ value	37
VI.2. Uncertainty with the Particle Data Group prescription	38
VI.3. Final $\alpha_s$ determination	39
VII. Conclusions	40
Acknowledgments	41
A. New LHC data sets included in the CT25 NNLO analysis	42

B. Sensitivity to charm-quark mass variations	44
References	45

## I. INTRODUCTION

The strong coupling constant  $\alpha_s$  is a fundamental parameter of the QCD Lagrangian that enters theoretical computations for all hadronic scattering processes. A precise and accurate determination of  $\alpha_s(Q)$  and its dependence on the energy scale  $Q$  is of vital importance for the current precision-frontier program at the Large Hadron Collider (LHC), where vast amounts of data are being gathered and push the boundary of precision measurements to the next level [1]. The upcoming high-luminosity phase of the LHC (HL-LHC) will further increase the volume of high-precision data, demanding a matching increase in both the detector capabilities and precision of theoretical calculations to properly validate relationships between fundamental parameters of the Standard Model (SM), constrain properties of the Higgs boson, and search for new physics interactions. For instance, the running of  $\alpha_s$  at the highest achieved energies may reveal the presence of new colored particles and influence the scale at which the SM couplings may unify. Variations in the observed  $\alpha_s(M_Z)$  at the scales of order of the mass of  $Z$  boson,  $M_Z$ , can affect projections for the range of energies at which the electroweak (EW) vacuum might shift from a metastable to a stable configuration.

Hence, the QCD coupling and its estimated uncertainty play a pivotal dual role of characterizing the universal force of nature and at the same time serving as a precise theoretical input for many standard candle processes in ongoing experiments. In particular, top-quark pair and Higgs boson production cross sections are very sensitive to the assumed  $\alpha_s(M_Z)$ : the associated uncertainty, entering at hadron colliders with the correlated PDF uncertainty, can potentially exceed those due to the scale dependence and experimental errors [2, 3].

The Particle Data Group (PDG) currently reports the uncertainty on  $\alpha_s(M_Z)$  of about 0.8% based on an analysis of combined world experimental data, resulting in  $\alpha_s(M_Z) = 0.118 \pm 0.0009$  [4]. The corresponding relative uncertainty exceeds those achieved for the fundamental couplings of electroweak and gravitational interactions. The new twist is that the latest determinations of  $\alpha_s$  from high-statistics experimental measurements and lattice QCD may individually quote a comparable, and soon a smaller, uncertainty than the PDG world-average uncertainty of  $\pm 0.0009$ . Along these lines, the ATLAS collaboration measured  $\alpha_s(M_Z) = 0.1183 \pm 0.0009$  [5] using data of  $Z$  boson transverse-momentum distributions at  $\sqrt{s} = 8$  TeV. The CMS collaboration simultaneously extracted  $\alpha_s(M_Z)$  and PDFs [6] from a global QCD analysis at NNLO using double-differential cross section measurements of inclusive jet produc-

tion at  $\sqrt{s} = 2.76, 7, 8$ , and  $13$  TeV combined with deep inelastic data from HERA. They obtained  $\alpha_s(M_Z) = 0.1176^{+0.0014}_{-0.0016}$ . Other recent relevant  $\alpha_s$  determinations from the CMS and ATLAS collaborations can be found in Refs. [5, 7–9]. Several determinations from deep inelastic scattering (DIS) at  $ep$  collider HERA find a somewhat lower  $\alpha_s$  value than at the LHC, such as  $\alpha_s(M_Z) = 0.1142 \pm 0.0028$  determined by H1 collaboration in a simultaneous fit of  $\alpha_s$  and proton PDFs [10]. Independently, lattice QCD determines  $\alpha_s$  from several types of nonperturbative computations. The Flavor Lattice Averaging Group (FLAG), systematizes and cross validates these determinations. It recently reports  $\alpha_s(M_Z) = 0.1183 \pm 0.0007$  [11].

The studies of  $\alpha_s$  thus enter a new phase when its accuracy can be potentially pushed to as low as 0.1% across diverse observations [1], while in the meantime novel challenges will need to be confronted both in the individual  $\alpha_s$  measurements and their combination. It is expected that, at this precision level, the growing complexity of involved systematic factors raises the chance for misestimations. When the misestimations go unnoticed – an unwanted common occurrence encountered in complex studies across many disciplines [12] – the uncertainty tends to be underestimated; some measurements of the parameter are not replicated by its independent determinations. When replicability degrades, a PDG or another combination may need to inflate the stated uncertainties of measurements in order to make them statistically compatible. As an illustration, the Committee on Data of the International Science Council inflates the errors of the highly precise measurements of the Newton’s gravitational constant  $G$  by a factor of 3.9 in order to meaningfully combine them [13]. Within its small span, the combined uncertainty band on  $G$  does not overlap significantly with those of several most precise measurements, meaning it does not replicate them. This indicates a general trend that the measurements of fundamental constants eventually experience the tradeoff between the precision and replicability, when raising the former depletes the confidence in the latter. How far can the precision measurements of  $\alpha_s$  go while remaining replicable? What can be done to control the uncertainty estimates and postpone the onset of non-replicability?

Our article will critically explore these questions on the case of the precision determination of the  $\alpha_s(M_Z)$  from the new CTEQ Tung Et Al. (CTEQ-TEA) global QCD analysis of nucleon scattering data, named “CT25” [14]. The primary goal of the global QCD analysis is to determine parametrizations of parton distribution functions (PDFs), as well as  $\alpha_s(M_Z)$  and other QCD parameters, from a simultaneous fit of a large, diverse collection of experimental measurements. The methodology of the global analysis offers the most complete look into the *correlated* constraints on  $\alpha_s$ , heavy-quark masses, and the PDFs arising from a variety of scattering experiments that *simultaneously* depend on them. This completeness gives the global analysis an edge over the standalone  $\alpha_s$  determinations from the nucleon data, which typically neglect at least some of the correlation with the PDFs or other experiments. As such, and

given the growing dominance of hadron scattering processes in experimental  $\alpha_s$  determinations, the global analysis of PDFs is well posed for tests of uncertainty quantification and replicability in the  $\alpha_s$  studies. Many combined analyses of the PDFs and  $\alpha_s$  have been performed by our CTEQ-TEA group [15, 16] and other groups [17–22] over the years. The strong coupling  $\alpha_s(M_Z)$  has recently been extracted from global QCD analyses, employing an approximate PDF evolution at the next-to-next-to-next-to-leading order (aN<sup>3</sup>LO) [23] in QCD by the MSHT group, and from an analysis using an aN<sup>3</sup>LO QCD evolution combined with the photon PDF at the next-to-leading order (NLO) in QED [24] by the NNPDF collaboration.

The CT25 global analysis determines  $\alpha_s$  at the next-to-next-to-leading order (NNLO) in QCD by employing an improved methodology as well as an extended global data set in which precision LHC Run-2 measurements with high integrated luminosity augment those included in the CT18 study [16]. The novel feature of our study is that we determine the central value and uncertainty of  $\alpha_s(M_Z)$  by several methods to obviate the dependence on the correlation with PDFs, selection of experiments, and systematic uncertainties in the experiments.

We do not resort to the definition of the PDF uncertainty (tolerance [25]) to estimate the allowed  $\alpha_s(M_Z)$  range, in contrast to the previous combined PDF+ $\alpha_s$  fits. Instead, we determine the span of the  $\alpha_s$  values consistent with the global data set at NNLO in several ways: (i) by generating the  $\chi^2(\alpha_s)$  profile from a single fit, (ii) by comparing the  $\alpha_s$  values from many fits with independent PDF parametrizations, and (iii) by combining the constraints from individual experiments according to several criteria to assess the uncertainty. The final  $\alpha_s(M_Z)$  result is obtained by combining several such extractions.

The rest of this manuscript is organized as follows. In Sec. II, we briefly describe the methodologies and advancements in the CT25 global PDF analysis. We summarize the new data sets included in the CT25 baseline, definition of the figure-of-merit function  $\chi^2$ , and implementation of correlated systematic errors provided by the experiments. Section III.1 explores the impact of the choice of PDF parametrizations on the  $\alpha_s$  determination. We also review how  $\alpha_s(M_Z)$  can be determined from the  $\chi^2$  scan over  $\alpha_s(M_Z)$ , and which criteria are applicable for determination of the  $\alpha_s(M_Z)$  and its error in this methodology.

Sec. III.2 critically examines the impact of the implementation of experimental systematic uncertainties on the extracted value of  $\alpha_s(M_Z)$ , and it discusses handling of some observed disagreements among data sets in the baseline. Section IV is dedicated to the exploration of uncertainty prescriptions (tolerances) according to the commonly used global and dynamical implementations. For the latter definition, we examine how the user-specified combination of published data sets into clusters modifies the quantitative error estimates. We point out that either the dynamical tolerance in the Hessian method or  $K$ -folding in the Monte-Carlo method may produce uncertainties that depend on user-chosen clustering of data sets.

We introduce the concept of data clustering safety that must be addressed in such situations.

Sec. V describes Bayesian statistical models utilized for the combination of the results for  $\alpha_s(M_Z)$  and its uncertainties, while Sec. VI obtains and compares the uncertainties using a variety of methods. This Section quotes our final  $\alpha_s$  estimate. Sec. VII contains our conclusions.

## II. RELEVANT ASPECTS OF THE CT25 GLOBAL ANALYSIS

### II.1. Selection of data sets

As many general-purpose CTEQ-TEA fits, the CT25 NNLO global analysis took place over several years and now culminates with the release of the official CT25 PDF ensembles that update the previous generation of the PDFs [16] consisting of the default CT18 NNLO error set and three alternative, yet equally acceptable PDF ensembles, CT18Z, A, and X. A significant part of this effort went into an exploration of a large number of new candidate measurements for the extension of the CT18 baseline data set, focusing primarily on high-precision production of lepton pairs, hadronic jets, and top quark-antiquark pairs in the LHC Runs 1 and 2. From many such examined data sets, we selected several precise and mutually consistent ones that we included into the final CT25 release. We documented these preliminary explorations in three publications [40–42].

These newly added LHC data sets in CT25 are listed in the upper part of Table I and reviewed in Appendix A. As its data baseline, CT25 started with the CT18A [16] global data set, which already included a combination of measurements in deep-inelastic scattering and production of lepton pairs, hadronic jets, and top-quark pairs at both fixed-target and collider energies. Notably, the CT18A baseline included a precision data set on  $W$  and  $Z$  production in the ATLAS experiment at 7 TeV [43], which offered the first evidence for the enhanced strangeness PDF at  $x \approx 0.02$ , in some disagreement with charged-current DIS experiments. The even more recent LHC measurements included in the CT25 fit are consistent with this strangeness enhancement.

The inclusion of the new LHC measurements, added on top of the CT18A baseline *without replacing or discarding any of the previously fitted experiments*, increased the number of data points,  $N_{\text{pt}}$ , by 769, the majority of which were from inclusive jet production and Drell-Yan triple-differential  $Z$ -boson production at ATLAS, cf. Table I. This version of the CT25 fit, which we will call “CT25prel”, has the largest  $N_{\text{pt}} = 4450$  among the various CT25 candidate fits. This data set is not unique, however: other well-motivated data combinations are possible, as was also in the CT18 case. When all data sets are retained in the CT25 baseline, we observe a reasonable, although not ideal, agreement among the global data, with significant pulls on the PDFs from the newly-fitted data. The most precise new

New experiments in the CT25 global fit			
ID	Experiment	$N_{\text{pt}}$	$\chi^2/N_{\text{pt}}$ for $\alpha_s(M_Z) = 0.118$ , CT25 (CT18A)
Lepton pair production			
211	ATLAS 8 TeV $W$ [26]	22	$2.04^{+0.65}_{-0.52}$ ( $4.35^{+2.65}_{-2.37}$ )
212	CMS 13 TeV $Z$ [27]	12	$2.02^{+1.03}_{-1.23}$ ( $2.12^{+3.77}_{-0.17}$ )
214	ATLAS 8 TeV $Z$ 3D [28]	188	$1.16^{+0.14}_{-0.06}$ ( $1.22^{+0.34}_{-0.14}$ )
215	ATLAS 5.02 TeV $W, Z$ [29]	27	$0.62^{+0.10}_{-0.09}$ ( $0.77^{+0.34}_{-0.09}$ )
217	LHCb 8 TeV $W$ [30]	14	$1.39^{+0.34}_{-0.23}$ ( $1.52^{+0.49}_{-0.36}$ )
218	LHCb 13 TeV $Z$ [31]	16	$1.09^{+0.49}_{-0.39}$ ( $1.24^{+1.03}_{-0.38}$ )
$t\bar{t}$ production at 13 TeV			
521	ATLAS all-hadronic $y_{t\bar{t}}$ [32]	12	$1.11^{+0.07}_{-0.07}$ ( $1.06^{+0.10}_{-0.07}$ )
528	CMS dilepton $y_{t\bar{t}}$ [33]	10	$1.28^{+0.43}_{-0.44}$ ( $1.04^{+0.78}_{-0.44}$ )
581	CMS lepton+jet $m_{t\bar{t}}$ [34]	15	$1.13^{+0.33}_{-0.31}$ ( $1.36^{+0.89}_{-0.48}$ )
587	ATLAS lepton+jet $m_{t\bar{t}} + y_{t\bar{t}} + y_{t\bar{t}}^B + H_T^{t\bar{t}}$ [35]	34	$1.07^{+0.19}_{-0.13}$ ( $0.94^{+0.24}_{-0.10}$ )
Inclusive jet production			
553	ATLAS 8 TeV IncJet [36]	171	$1.60^{+0.10}_{-0.06}$ ( $1.57^{+0.12}_{-0.07}$ )
554	ATLAS 13 TeV IncJet [37]	177	$1.32^{+0.06}_{-0.05}$ ( $1.26^{+0.09}_{-0.03}$ )
555	CMS 13 TeV IncJet [38]	78	$1.10^{+0.10}_{-0.05}$ ( $1.12^{+0.17}_{-0.13}$ )
All experiments			
PDF ensemble		$N_{\text{pt}}$	$\chi^2/N_{\text{pt}}$ for $\alpha_s(M_Z) = 0.118$ Preferred $\alpha_s(M_Z)$
CT25 NNLO, with default data set [14]		4066	$1.20 \pm 0.009$ $\approx 0.1185$
CT25prel, with augmented CT18A data set		4450	$1.20 \pm 0.010$ $\approx 0.118$
CT18A NNLO [16]		3674	$1.19 \pm 0.013$ $\approx 0.1165$

TABLE I. The upper part of the table lists the newly added data sets in the CT25 analysis, contributed by measurements in lepton-pair, top-quark pair, and single-inclusive jet production from the LHC Runs 1 and 2. They contain  $N_{\text{pt}} = 769$  new data points in total. For these experiments, we report the  $\chi^2/N_{\text{pt}}$  for the default CT25 and prior CT18A PDF ensembles, assuming  $\alpha_s(M_Z) = 0.118$ . Section II.2 provides the definition of  $\chi^2$ . The errors are asymmetric PDF uncertainties computed with a master formula in Ref. [39], and with the error PDFs defined at 68% CL according to the two-tier PDF tolerance employed in CT18. The lower part of the table shows the total numbers of points,  $\chi^2/N_{\text{pt}}$ , and approximate preferred  $\alpha_s(M_Z)$  in the default and preliminary CT25 fits described in the text, as well as in the CT18A fit.

experiments in the CT25 fits tend to exhibit an increase in  $\chi^2/N_{\text{pt}}$  in a pattern similar to that observed in the CT18 global analysis. The new Drell-Yan and  $t\bar{t}$  production data consistently prefer a softer gluon at intermediate-to-large  $x$  ( $0.05 \leq x \leq 0.7$ ), while jet production data pull the gluon in the opposite direction in the same kinematic range. Overall, the cumulative effects of these measurements, when they are combined, amounts to having a softer gluon at the intermediate-to-large  $x$ , as compared to CT18A.

To representatively investigate the range of PDF solutions in this new setting, we explored other descendant, also acceptable, branches of the CT25prel fit. The alternative choices made in these fits reflect the complexities present within the global fitting framework, many of which were highlighted in the preceding CT18 publication [16], as well as in a review [25].<sup>1</sup> In the end, we obtained the default CT25 fit, or just “CT25”, as follows. Compared to CT18A and CT25prel, we replaced the H1 measurements of charm and bottom semi-inclusive structure functions [44, 45] by their HERA combination [46], which moderately increased the corresponding  $\chi^2$  without substantially modifying the PDFs. We added the E906/SeaQuest measurement of the  $\sigma_{pd}/(2\sigma_{pp})$  ratio in fixed-target Drell-Yan pair production [47]. We removed four data sets (336 points) on inclusive charged-current DIS on an iron target from the CDHSW [48] and CCFR [49, 50] collaborations, as they are in some tension with each other and increase dependence of CT25 results on the nuclear modifications of proton PDFs.<sup>2</sup> The weakly sensitive determination of the longitudinal structure function  $F_L(x_B, Q^2)$  by the H1 collaboration [52] was also omitted without a noticeable impact on the PDFs.

Turning back to Table I, the last column in its upper part reports the ratios the  $\chi^2/N_{\text{pt}}$  values for each listed experiment using the PDFs from the default CT25 NNLO and CT18A NNLO global fits (with the latter in parentheses). The errors express the corresponding asymmetric PDF uncertainties that are evaluated at the 68% credibility level (CL).<sup>3</sup> Fitting the new experiments in the CT25 framework generally improves their  $\chi^2$ .

The lower part of Table I compares the total numbers of points and  $\chi^2/N_{\text{pt}}$  for the default CT25, CT25prel, and their CT18A predecessor. The last column of the lower part also shows the *approximate* preferred value of  $\alpha_s(M_Z)$  in these three fits, which is further adjusted by modifications discussed in the rest of the article.

Upon the addition of the LHC data sets in CT25prel, the reference  $\alpha_s(M_Z)$  increased from a range 0.1164-0.1169 in the CT18 series to  $\approx 0.118$ . To a large extent, this change is due to the preference for a softer gluon at the intermediate-to-large  $x$ , which is compensated by some increase in  $\alpha_s(M_Z)$ .

<sup>1</sup> In the context of CT18, we opted to publish four PDF ensembles to quantify some of these possibilities.

<sup>2</sup> The default CT25 fit nevertheless retains CCFR and NuTeV data sets on dimuon production in CC DIS on the isoscalar target, as those provide unique constraints on the strangeness PDF at  $x > 0.05$ . In both CT18 and CT25 fits, we apply a correction from [51] to approximate nuclear modifications in such experiments.

<sup>3</sup> The PDF fits base themselves on the Bayesian paradigm, and hence the interpretation of their errors on the PDFs and  $\alpha_s$  as “credibility intervals” is appropriate. That said, these errors are also used to predict the frequency of future measurements using the determined parameters, in which case the users may view them as “confidence intervals”.

In the default CT25 fit, the reference  $\alpha_s(M_Z)$  is further increased to  $\approx 0.1185$  primarily because of the exclusion of the CDHSW inclusive charged-current DIS data set [48] on iron. The exclusion of the counterpart CCFR measurement had no appreciable effect. In the CT18 publication, we emphasized that the CDHSW data set is generally fitted well, yet its  $Q$  dependence differs from that of an analogous CCFR observation [53], which in turn may reflect differences in calibration and resolution of the two detectors [54]. The Lagrange Multiplier scans in the context of CT18 (see its Fig. 21) showed that CDHSW prefers a far larger gluon  $g(x, Q)$  at  $x > 0.1$  than the other experiments. This preference, in turn, suppresses the preferred  $\alpha_s(M_Z)$ . For this reason, the two CDHSW data sets were included in CT18/CT18A/CT18X, but not in CT18Z. Either way, the impact of adding or removing the inclusive neutrino-iron DIS data sets is weak and comparable to other less known factors. The  $\chi^2/N_{\text{pt}}$  is smaller when these CDHSW and CCFR experiments are included, so they do not manifestly disagree with the rest.

Our general observation is then that the described revisions in the CT25 data set, as compared to the CT18A one, tend to elevate the preferred  $\alpha_s(M_Z)$  to above 0.118 *for the default settings of the global fit*. We should next emphasize that this trend may change considerably under reasonable modifications in the fit’s settings, reflecting in part *inconsistencies (tensions) among the input data sets*, and in part the *modeling of experimental and theoretical systematic uncertainties*.

## II.2. The CTEQ-TEA goodness-of-fit function

In the exploration of uncertainties, we will repeatedly turn to the goodness-of-fit (GOF) function  $\chi^2 \equiv -2 \ln P(T|D)$ , minimized with respect to all free parameters in the fit to maximize the posterior probability  $P(T|D)$ . The CT25 analysis implements it as

$$\chi^2 = \chi_R^2 + \chi_{\text{LM}}^2, \quad (2.1)$$

where  $\chi_R^2$  quantifies the agreement of theory with experiments, and  $\chi_{\text{LM}}^2$  is a generally small contribution imposing theoretical priors on the PDFs. The latter is constructed from Lagrange-Multiplier (LM) contributions whose role is to (i) enforce physical behavior of PDF flavor ratios in the extrapolation regions with poor constraints from the data and (ii) enable a “ridge” (L2) regularization on a few poorly constrained, yet correlated PDF parameters.

In a fit with  $N_E$  data sets, the first term in Eq. (2.1),

$$\chi_R^2 \equiv \sum_{E=1}^{N_E} \chi_E^2, \quad (2.2)$$

is a sum of contributions  $\chi_E^2$  from individual data sets  $E$  given by [16, 39]

$$\chi_E^2(\mathbf{a}, \boldsymbol{\lambda}, \alpha_s(M_Z), \{m_q\}) = \sum_{k=1}^{N_{\text{pt}}^{(E)}} \frac{1}{s_k^2} \left( D_k - T_k(\mathbf{a}, \alpha_s(M_Z), \{m_q\}) - \sum_{\alpha=1}^{N_{\lambda}^{(E)}} \beta_{k\alpha}(\mathbf{a}, \alpha_s(M_Z), m_q) \lambda_{\alpha} \right)^2 + \sum_{\alpha=1}^{N_{\lambda}^{(E)}} \lambda_{\alpha}^2. \quad (2.3)$$

Here  $D_k$  and  $T_k$  are the  $k$ -th central experimental and theory values, respectively,  $s_k = \sqrt{s_{k,\text{stat}}^2 + s_{k,\text{uncor}}^2}$  is the total uncorrelated error on the measurement  $D_k$ , and  $\beta_{k\alpha}^{(E)}$  is the correlation matrix of systematic uncertainties.  $\mathbf{a} \equiv \{a_1, a_2, \dots, a_{N_{\text{pdf}}}\}$  and  $\boldsymbol{\lambda} \equiv \{\lambda_1, \dots, \lambda_{N_{\lambda}^{(E)}}\}$  are the vectors of PDF parameters and systematic nuisance parameters of  $E$ , with the latter commonly assumed to be random and distributed according to a standard normal distribution  $\mathcal{N}(0, 1)$ . Equation (2.3) indicates that  $\chi^2$  generally depends on QCD parameters –  $\alpha_s(M_Z)$  and quark masses  $m_q$  – both through the theoretical predictions  $T$  and the experimental correlation matrices  $\beta_{k\alpha}$ , although this dependence of the latter is usually neglected.

In our study, we minimize the total  $\chi^2$  with respect to  $\alpha_s(M_Z)$  and  $\mathbf{a}$ , while using constant  $\{m_q\}$  and profiling [55] the nuisance parameters  $\boldsymbol{\lambda}$  for every  $\{\alpha_s, \mathbf{a}\}$  combination. We will find it helpful that, at its global minimum for each  $\alpha_s(M_Z)$ , the  $\chi^2$  can be expressed in terms of the best-fit PDF parameter combination  $\mathbf{a}_0$  as (see Eq. (B8) in [16])

$$\min_{\mathbf{a}} \chi^2(\mathbf{a}, \alpha_s(M_Z), \{m_q\}) \equiv \chi^2(\mathbf{a}_0, \alpha_s(M_Z), \{m_q\}) = \sum_E \left[ \underbrace{\sum_{k=1}^{N_{\text{pt}}^{(E)}} [r_{0,k}^{(E)}]^2}_{\equiv D^2} + \underbrace{\sum_{\alpha=1}^{N_{\lambda}^{(E)}} [\lambda_{0,\alpha}^{(E)}]^2}_{\equiv R^2} \right], \quad (2.4)$$

i.e., it is a quadrature sum of the best-fit data residuals  $r_{0,k}^{(E)}$  and best-fit nuisance parameters for each experiment  $E$ . Their explicit formulas are [16]

$$r_{0,k}^{(E)} = \frac{1}{s_k} \left( D_k - T_k(\mathbf{a}_0) - \sum_{\alpha=1}^{N_{\lambda}^{(E)}} \beta_{k\alpha} \lambda_{0,\alpha}^{(E)} \right), \text{ and} \quad (2.5)$$

$$\lambda_{0,\alpha}^{(E)} = \frac{1}{s_k^2} (D_k - T_k(\mathbf{a}_0)) \beta_{k\gamma} \mathcal{A}_{\gamma\alpha}^{-1}, \text{ with } \mathcal{A}_{\alpha_1\alpha_2} = \delta_{\alpha_1\alpha_2} + \sum_{k=1}^{N_{\text{pt}}^{(E)}} \frac{\beta_{k\alpha_1} \beta_{k\alpha_2}}{s_k^2}, \quad (2.6)$$

and all terms on the right-hand side corresponding to experiment  $E$ . Furthermore, since  $r_{0,k}^{(E)}$  and  $\lambda_{0,\alpha}^{(E)}$  are correlated only through a relatively small number of PDF parameters, especially across separate experiments, in the first approximation they all can be assumed to be independently and normally distributed,  $r_{0,k}^{(E)} \sim \mathcal{N}(0, 1)$  and  $\lambda_{0,\alpha}^{(E)} \sim \mathcal{N}(0, 1)$ . This independence opens the possibility of reclustering the individual data points in the total  $\chi^2$  in Eq. (2.4), which will be pursued in Sec. IV. Furthermore, in Sec. IV.4 we can examine separate reclustering of sums of all best-fit residuals and nuisance parameters, denoted as  $D^2$  and  $R^2$ , respectively.

### II.3. Limitations of existing models for correlated systematics

Several aspects of the implementation of correlated systematic errors using  $\beta_{k\alpha}$  in our  $\chi^2$  will be relevant for the interpretation of the results that will follow.

1. We first note that the total number  $N_\lambda$  of the experimental nuisance parameters has grown from at most a few tens in the early global fits to more than 2000 in the CT25 analysis. That is,  $N_\lambda$  is now close to a half of the total data points  $N_{\text{pt}}$  due to the tendency of the latest experiments to provide large correlation or covariance matrices.
2. While the common uncertainty estimates in the PDF fits operate in the traditional central limit applicable when the number of data,  $N_{\text{pt}}$ , is much larger than the number of parameters  $N_{\text{par}}$ , the reality of the latest fit is that its total  $N_{\text{par}} = N_{\text{pdf}} + N_\lambda$  and  $N_{\text{pt}}$  are comparable. The central limit estimates may receive corrections of order  $N_{\text{par}}/N_{\text{pt}}$ , which are currently not considered in the PDF analyses.
3. Considerable attention has been recently paid to the fact that, by using the linear Gaussian models to publish their correlated systematic uncertainties, experiments unavoidably leave significant information out of the scope accessible within the PDF fit. There are a couple such points, first, related to the standard assertion that all systematic nuisance parameters follow the standard normal distribution,  $\lambda_\alpha^{(E)} \sim \mathcal{N}(0, 1)$  in the  $\chi^2$  definition in Eq. (2.3). Not only it is highly unlikely that all  $\lambda_\alpha$  parameters will be thusly distributed, there are known important cases when this assumption is false, e.g., for so-called two-point uncertainties that take the difference of at most two estimates, for instance, provided by two parton shower programs, as a measure of a possible uncertainty.
4. The second point of the information loss emerges from the common practice of publishing only *normalized* correlation matrices,  $\sigma_{k\alpha}$ , from which the actual correlation matrices,  $\beta_{k\alpha} = X_k \sigma_{k\alpha}$  in Eq. (2.3), must be reconstructed by multiplying by unspecified reference values  $X_k$  that are chosen within the PDF fit itself. The  $X_k$  values are of order of either the central data values,  $D_k$ , or respective theoretical values,  $T_k$ . They don't need to coincide with either; the prescription for choosing  $X_k$  is a delicate part of the fitting model [56, 57], approached differently by each PDF fitting group, who try to reasonably fill the lacunas in the correlation models they get.

How do these considerations impact the precise determination of the QCD coupling constant? We address this question in the next section, after discussing another potential source of uncertainty due to the freedom in the PDF parametrization.

### III. SOURCES OF UNCERTAINTIES ON QCD COUPLING

#### III.1. The PDF parametrization uncertainty is small...

It has been pointed out over years, e.g., in [15, 16, 58, 59], that QCD parameters determined from a global fit are mutually dependent with the PDFs and thus must be fitted simultaneously with the PDFs. Within the global fit, the correlation between the  $\alpha_s(M_Z)$  and PDFs can be captured either by fitting them together or by scanning the  $\chi^2(\alpha_s(M_Z), \vec{a}_0)$  over  $\alpha_s(M_Z)$ , while minimizing the  $\chi^2$  with respect to the PDFs for each  $\alpha_s(M_Z)$  value. Either approach can be used to determine the best-fit combination of  $\alpha_s(M_Z)$  and PDFs together with their uncertainties. We will employ both approaches, especially the latter one – the  $\alpha_s$  scan – to elucidate such combined fits.

Our study suggests a low correlation of the best-fit  $\alpha_s(M_Z)$  with the functional forms of PDF parametrizations in the vicinity of the overall global  $\chi^2$  minimum. The consequence is that the choice of the PDF parametrizations has a low impact on the  $\alpha_s(M_Z)$  and its error, among the candidate functional forms of the CT25 fit that render the lowest achieved values of  $\chi^2$ . The variation of the best-fit  $\alpha_s(M_Z)$  caused by the choice of the parametrization forms is comparable with the uncertainty corresponding to a  $\Delta\chi^2 = 1$  change in the global  $\chi^2$ . We will see that this is quite a small uncertainty, compared to other sources.

Figure 1 illustrates the low correlation of best-fit  $\alpha_s(M_Z)$  and PDFs by comparing the  $\chi^2$  dependence from an  $\alpha_s(M_Z)$  scan for the functional forms of the nominal CT25 fit and 287 fits with alternative PDF parametrizations explored as a part of the full CT25 exercise. In this plot, we focus on the component of the total  $\chi^2$  consisting from experimental log-likelihoods and denoted by  $\chi_R^2$  as in Eq. (2.1), and neglecting the prior component  $\chi_{LM}^2$  that is relatively constant in this comparison. All fits in this figure are done with identical settings that are close both to the CT25prel and final CT25 ones introduced in Sec. II.1. Namely, the shown fit with the nominal CT25 parametrization achieves  $\min \chi_R^2 \equiv \chi_0^2 = 5087$  for  $N_{\text{pt}} = 4260$  data points. Compared to the CT25prel fit, it excludes the CDHSW heavy-nucleus CC DIS data set [48], which prefers a low  $\alpha_s(M_Z)$ , as well as the weakly sensitive H1  $F_L$  data set [52]. It retains other experiments of the CT25prel baseline.

The orange star in Fig. 1 indicates the best-fit combination  $\{\alpha_s \approx 0.1185, \chi_R^2 = 5087\}$  obtained with the nominal CT25 parametrization. The approximately parabolic orange curve indicates the  $\chi_R^2$  dependence from the  $\alpha_s$  scan with this parametrization. The vertical magenta band indicates the interval of  $\alpha_s(M_Z)$  values corresponding to the increase  $\Delta\chi_R^2 \leq 1$  from the  $\alpha_s$  scan, measured with respect to the minimal  $\chi_R^2$  on this quasi-parabola.

The blue dots indicate the best-fit  $\{\alpha_s(M_Z), \chi_R^2\}$  combinations from simultaneous PDF+ $\alpha_s$  fits that

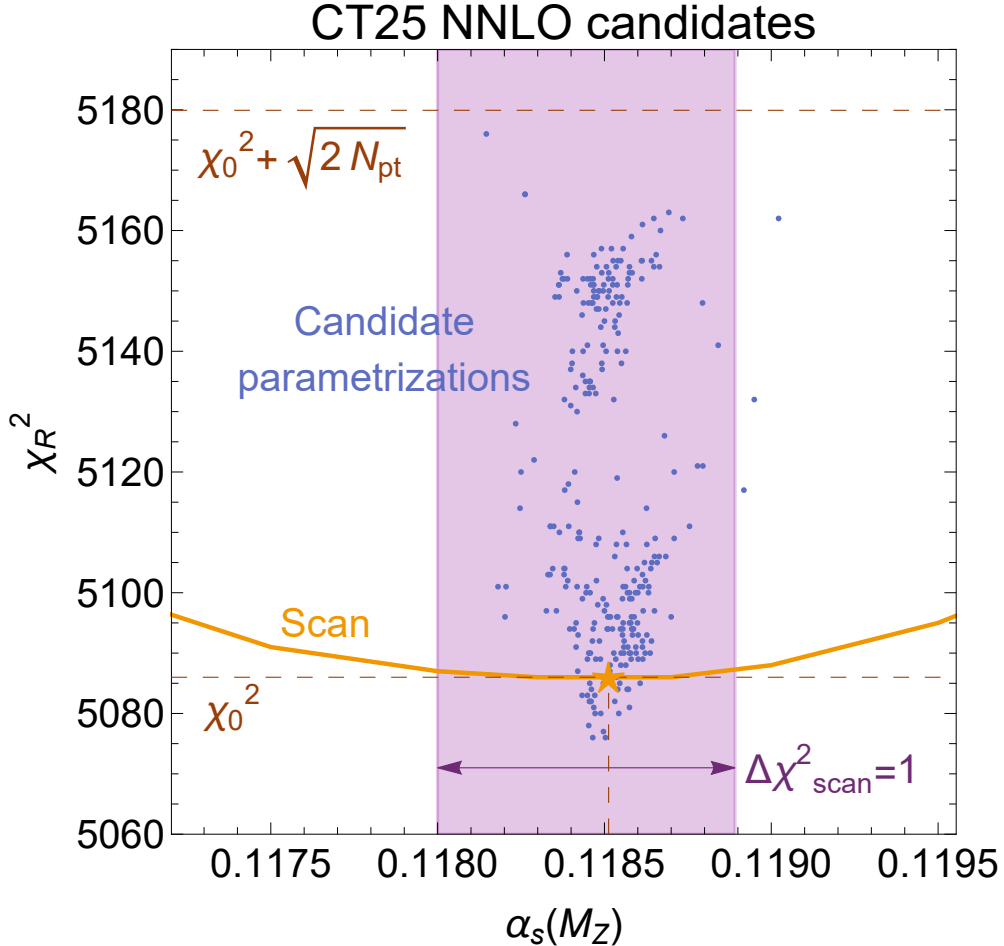


FIG. 1.  $\chi^2$  of the data versus  $\alpha_s(M_Z)$  from the scan of the nominal CT25 PDF parametrization form and PDF+ $\alpha_s$  fits with 287 alternative parametrizations.

use 287 variants of PDF parametrization forms. In these parametrizations, both the functional forms and number of parameters are varied. A small number of candidate fits in Fig. 1 have a lower  $\chi_R^2$  (slightly better agreement with data) than the nominal CT25 parameterization (the orange star). Yet they have a slightly worse overall  $\chi^2$  due to the additional LM penalties in the extrapolation regions, e.g. because they result in less physical asymptotic behaviors of (anti-)quark PDFs in the far  $x \rightarrow 1$  limit. On the side of the upper  $\chi_R^2$ , we show only the candidate parametrizations that have only a modestly higher  $\chi_R^2$  compared to  $\chi_0^2$  of the nominal fit. Namely, we show the fits whose  $\chi_R^2$  is less than  $\chi_0^2 + \sqrt{2N_{\text{pt}}}$ , i.e., fall within the 68% CL of the statistical uncertainty on  $\chi_R^2$  of the nominal fit. Such candidate solutions are a priori eligible for inclusion into the final  $\alpha_s$  average over PDF models, even though they will be included with a lower weight into the model average because of their elevated  $\chi_R^2$ 's.

Here we observe a striking behavior: while the  $\chi^2$  variations among the candidate fits are sizable in the vertical ( $\chi^2$ ) direction, they have modest horizontal variations, compatible with the size of the  $\Delta\chi^2 = 1$

interval, as far as the best-fit  $\alpha_s(M_Z)$  are concerned. The picture immediately reminds of the textbook case of the  $\chi^2$  variability due to approximately Gaussian random fluctuations in data [60]: when one plots the log-likelihood ( $\chi^2$ ) vs. the parameter of interest ( $a$ ), vertical fluctuations of the resulting parabola fall into the interval  $\chi_R^2 \leq \chi_0^2 + \sqrt{2N_{\text{pt}}}$  in  $\approx 68\%$  of cases, while about 68% of the horizontal fluctuations fall within the interval  $\Delta\chi_R^2 \leq 1$ .

In our example, the best-fit  $\alpha_s(M_Z)$  from fits with alternative parametrizations fall within the interval for  $\Delta\chi_R^2 = 1$  from the scan, reflecting statistical fluctuations in the data at 68% CL for the fixed data set and PDF functional forms. This interval corresponds to the uncertainty  $\delta\alpha_s \approx \pm 0.0005$ , and this conclusion holds for other candidate selections of baseline experiments. Namely, while the preferred  $\alpha_s(M_Z)$  value moves between  $\approx 0.1175$  and  $0.1185$  for the CT25prel and CT25 selections of data sets, see the bottom of Table I, the pattern of the parametrization dependence is about the same in these fits as in Fig. 1, with the parametrization uncertainty staying at the level of 0.0005.

The conclusion based on the ensemble of nearly 300 PDF parametrizations is then that they give very similar  $\alpha_s(M_Z)$  values, showing that the determination of  $\alpha_s(M_Z)$  is essentially independent of the chosen PDF parametrization. If only this source of uncertainty were considered, the uncertainty span of approximately  $\pm 0.0005$  about the central value would be smaller than the PDG uncertainty [61] of  $\pm 0.0009$  and even dedicated PDF-only fits [16, 17, 19, 20, 62–64] quoting errors of order  $\pm 0.002$ .

### III.2. ...but the systematic uncertainty remains

The global fit contains two more significant sources of  $\alpha_s$  variations, introduced by the dependence on the models of correlated systematic errors already brought up in Sec. II.3, as well as by the more-than-normal disagreements between the parts of the hadronic data set. This section will address the first aspect and illustrate the possible impact of the choice of the reference normalization factors  $X_k$  in the experimental correlation matrices  $\beta_{k\alpha} = X_k \sigma_{k\alpha}$ , which is controlled in our fit by the parameter `ksys`. Section IV will follow with addressing the second aspect.

Since the experiments normally do not publish their recommended  $X_k$ , a variety of “guesses” about  $X_k$  can be, and have been, made in the past PDF fits [56, 57]. As illustrative possibilities, we consider two such prescriptions, which we label as “`ksys=1`” and “`ksys=2`”. According to the `ksys=1` prescription, each correlated systematic element  $\beta_{k\alpha}$  (initially provided as a percentage fraction  $\sigma_{k\alpha}$ ) is normalized to the current theory prediction  $T_k$  for each data point. This treatment is more suitable when the corresponding experimental error is multiplicative. On the other hand, it can potentially introduce a theory bias in the effect of systematic errors. The majority of fits by CTEQ-TEA and other groups choose `ksys=1` for all correlated errors as a default.

The `ksys=2` prescription, instead, normalizes the correlated systematic element to the experimental central value  $D_k$ . It is most suitable for normalizing additive errors. It can potentially lead to a large D'Agostini bias [65–67] (characteristically producing a downward bias in the best-fit cross section) when the underlying error is multiplicative.

For the ensuing discussion, we divide our baseline data set of measurements into three subsets: 1) deep-inelastic scattering (DIS), 2) Drell-Yan (DY) pair production, 3) inclusive jet and  $t\bar{t}$  production. In each subset, we normalize all  $\beta_{k\alpha}$  as though they are multiplicative (`ksys=1`) or additive (`ksys=2`). In reality, most measurements contain a mix of multiplicative and additive errors. The true value of  $\alpha_s(M_Z)$  extracted from the global fit is somewhere between the extremes corresponding to the “all `ksys=1`” and “all `ksys=2`” options. This setup allows us to explore sensitivity to systematic error modeling, particularly for hadron jet production observables that exhibit a very large sensitivity.

We first demonstrate what happens in the final CT25 fit when we change the default setting of using “`ksys=1`” in all three measurement categories, labeled as  $\{\text{ksys}_{\text{DIS}}, \text{ksys}_{\text{DY}}, \text{ksys}_{\text{Jet+}t\bar{t}}\} = \{1, 1, 1\}$ . First, to illustrate how the `ksys` choice modifies  $\chi^2$  when all other settings are unchanged, let us examine the  $\chi^2$  dependence for several combinations of `ksys` values *while using the same PDF ensemble*. Figure 2 illustrates these changes, by showing  $\chi^2$  vs  $\alpha_s$  using the nominal CT25 data set and best-fit PDFs for

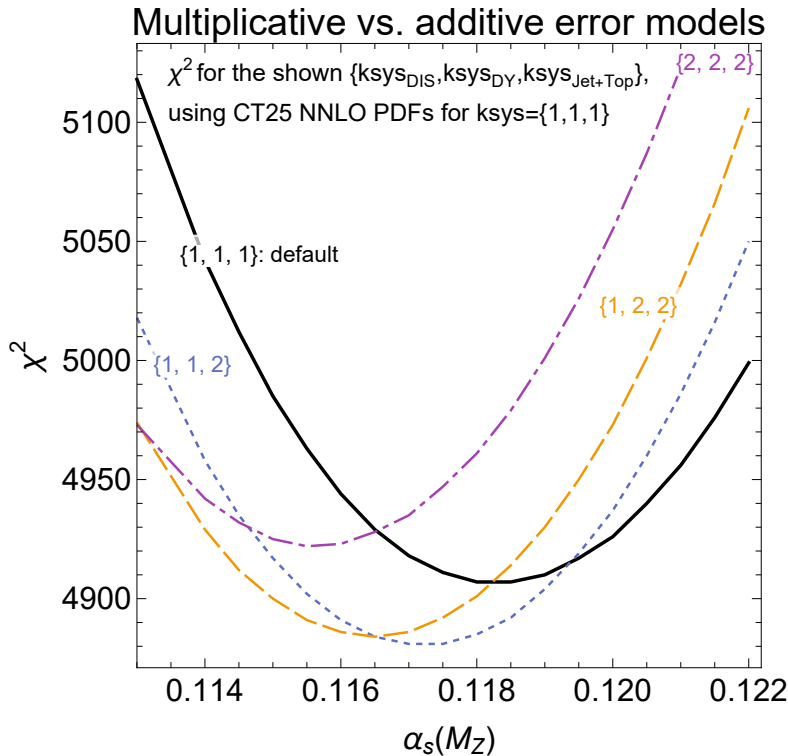


FIG. 2.  $\chi^2$  profiles for different `ksys` settings:  $\{\text{ksys}_{\text{DIS}}, \text{ksys}_{\text{DY}}, \text{ksys}_{\text{Jet+}t\bar{t}}\} = \{1, 1, 1\}$ ,  $\{1, 1, 2\}$ ,  $\{1, 2, 2\}$ , and  $\{2, 2, 2\}$ . These are obtained with a fixed CT25 PDF set determined with the default `ksys=1` setting.

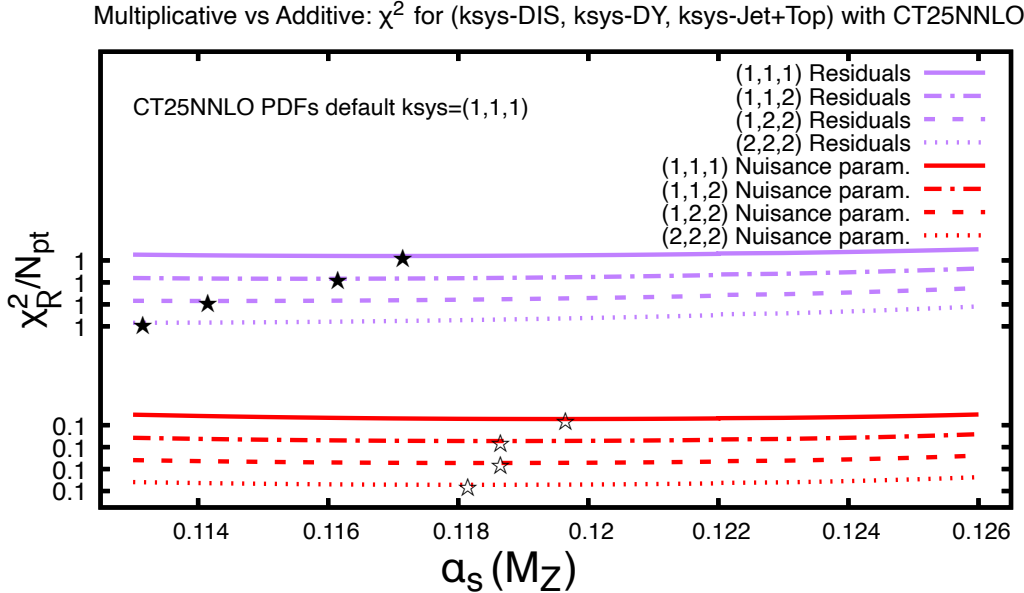


FIG. 3. Separate contributions to  $\chi^2_R/N_{\text{pt}}$  from the best-fit summed data residuals and nuisance parameters, as exemplified in Eq. 2.4, for the four `ksys` combinations shown in Fig. 2. The theory predictions are obtained with the CT25NNLO PDFs determined using `ksys`= $\{1,1,1\}$ .

$\{1,1,1\}$ , while computing the shown  $\chi^2$  respectively with  $\{1,1,1\}$ ,  $\{1,1,2\}$ ,  $\{1,2,2\}$ , and  $\{2,2,2\}$  `ksys` choices.

Both the minimal  $\chi^2$  and best-fit  $\alpha_s$  values change according to the `ksys` choices, covering the ranges of 4880-4530 and 0.1155-0.1185, respectively. The minima of the parabolas in this case correspond to the following  $\alpha_s(M_Z)$  values:  $\{1,1,1\} \rightarrow 0.1185$ ,  $\{1,1,2\} \rightarrow 0.1172$ ,  $\{1,2,2\} \rightarrow 0.1162$ , and  $\{2,2,2\} \rightarrow 0.1155$ . Already the change from `ksys`=1 to 2 for jet+ $t\bar{t}$  data sets only incurs a significant downward  $\alpha_s$  shift, which is further amplified by using `ksys`=2 for the other two groups of processes.

It is interesting to delve into details of the fits to understand the driving mechanism of these shifts. First, it appears that the shifts are largely driven by the decrease in the average of data point residuals and less by the best-fit nuisance parameters. This can be seen from Fig. 3 that separately plots the contributions from the best-fit residuals and nuisance parameters, given respectively by two sums on the right-hand side of Eq. 2.4, from the same four  $\alpha_s$  scans with the fixed  $\{1,1,1\}$  PDF as in Fig. 2. The curves from the four scans are stacked on the top of one another so as to fit in the figure. Stars indicate the minima of their corresponding parabolas. Positions of the stars for residuals can go as low as to  $\alpha_s(M_Z) = 0.113$  for the  $\{2,2,2\}$ . The stars for the nuisance parameters are more stable between 0.118 and 0.120.

Figures 4 and 5 depict this dynamics in the complete  $\alpha_s$  scans, now done using the CT25prel baseline

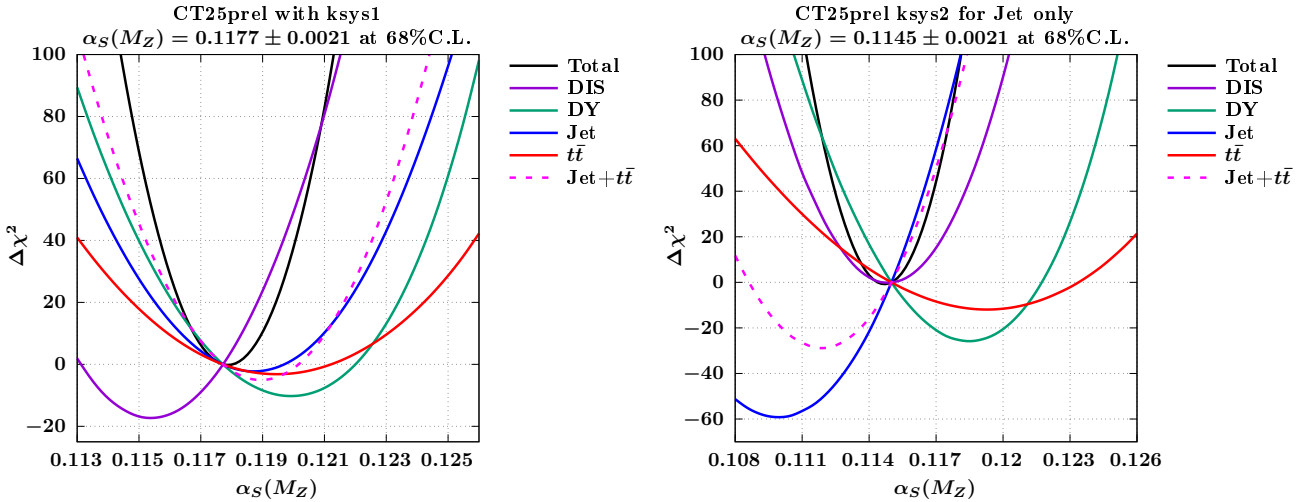


FIG. 4.  $\Delta\chi^2$  profiles vs.  $\alpha_s(M_Z)$  for the `ksys=1` (left) and `ksys=2` (right) prescriptions. Curves are shown for the full-baseline global fit (black), DIS (purple), DY (green), jets (blue),  $t\bar{t}$  (red), and jet+ $t\bar{t}$  (dashed magenta). Each parabola is obtained from the same global fit result, projected onto the corresponding data subset.

data set that prefers a slightly lower  $\alpha_s(M_Z) < 0.118$ . In these figures, the PDFs are fitted for the indicated `ksys` and  $\alpha_s(M_Z)$ .

Figure 4 illustrates the  $\Delta\chi^2 \equiv \chi^2_R(\alpha_s(M_Z)) - \chi^2_{R,0}$  profiles, as functions of  $\alpha_s(M_Z)$ , for six different clustering configurations of the data: the full baseline (black line), DIS (purple), Drell–Yan pair (green), inclusive jet (blue), and  $t\bar{t}$  production (red), as well as the combined jet+ $t\bar{t}$  data (dashed magenta). Each profile is obtained from the same global fit. The reference value,  $\chi^2_{R,0}$ , is the minimum  $\chi^2_R$  with respect to both  $\alpha_s(M_Z)$  and PDFs. The curves show  $\Delta\chi^2$  – the changes compared to  $\chi^2_{R,0}$  – for each indicated data cluster. By construction, all  $\Delta\chi^2$  curves intersect (are equal to zero) at the best-fit  $\alpha_s(M_Z)$  of the global fit. The minima of the parabolas represent the preferred  $\alpha_s(M_Z)$  values for each group of processes.

With the CT25prel baseline, the default global fit, using the `ksys=1` treatment (left panel), gives

$$\alpha_s(M_Z) = 0.1177 \pm 0.0021 \quad (68\% \text{ CL}), \quad (3.1)$$

where the 68% CL is computed according to  $\Delta\chi^2 = 37$ , the increase in the global  $\chi^2$  consistent with the CT18 tolerance definition. This  $\alpha_s(M_Z)$  value is in a good agreement with the current world average. At the same time, we observe that the preferred  $\alpha_s(M_Z)$  values vary across the processes. For example, the DIS experiments prefer the lowest value ( $\alpha_s(M_Z) = 0.1152$ ). Drell–Yan pair and top-quark pair production prefer higher values, 0.1198 and 0.1194, respectively. Inclusive jet production prefers an intermediate value ( $\alpha_s(M_Z) = 0.1187$ ). The spread of preferences in Fig. 4 (left) reflects the differing pulls on  $\alpha_s(M_Z)$  from various experiments and highlights tensions in the data.

When the `ksys=2` prescription is applied to the jet data in Fig. 4 (right), the global minimum of total

$\chi^2_R$  prefers a much lower  $\alpha_s(M_Z)$  value,

$$\alpha_s(M_Z) = 0.1145 \pm 0.0021 \quad (68\% \text{ CL}). \quad (3.2)$$

Refitting the PDFs results in an even larger downward shift of the preferred  $\alpha_s(M_Z)$  with `ksys=2` then when the PDFs were fixed in the previous exercise.

In this scenario, the ordering of preferred values is markedly different: jet production measurements favor by far the smallest value ( $\alpha_s(M_Z) = 0.1099$ ), while  $t\bar{t}$  production still pulls toward the largest value ( $\alpha_s(M_Z) = 0.1191$ ), and the DIS ( $\alpha_s(M_Z) = 0.1146$ ) and Drell–Yan process ( $\alpha_s(M_Z) = 0.1187$ ) lying in-between. Compared to the `ksys=1` case, the pull from jet-production measurements to a significantly lower value of  $\alpha_s(M_Z)$  is accompanied by an equally significant reduction in  $\chi^2$ , which reflects strong sensitivity of these measurements to the treatment of correlated systematics.

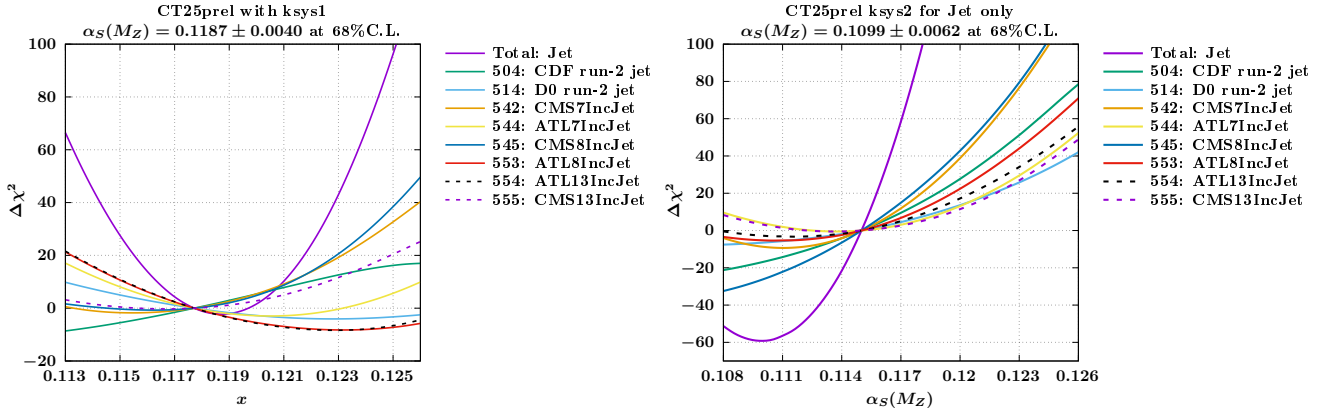


FIG. 5.  $\Delta\chi^2$  profiles for individual jet-production measurements only in the  $\alpha_s$  scans with the `ksys=1` (left) and `ksys=2` (right) prescriptions for jet data sets. The  $\alpha_s(M_Z)$  values in the plot headers are for the jet data subset only.

To further investigate the differences between the `ksys=1` and `ksys=2` scenarios in the case of inclusive-jet production measurements, Fig. 5 separately illustrates the  $\Delta\chi^2$  profiles of individual jet experiments. As before, the curves have  $\Delta\chi^2 = 0$  at the best-fit  $\alpha_s(M_Z)$  of the respective global fit. The `ksys=1` case is shown in the Fig. 5 (left), where the DØ Run-2 and ATLAS measurements at 7, 8, and 13 TeV collision energies prefer relatively large  $\alpha_s(M_Z)$ , while the CDF Run-2 and CMS measurements at 7, 8, and 13 TeV prefer smaller values. Their interplay produces a combined  $\alpha_s(M_Z)$ -minimum from jet production that is

$$\alpha_s(M_Z) = 0.1187 \pm 0.0040 \quad (68\% \text{ C.L.}), \quad (3.3)$$

and is consistent with the world average.

By contrast, when the `ksys=2` treatment is applied to jet data sets in Fig. 5 (right), all of them prefer a much smaller  $\alpha_s(M_Z)$ . The CMS 8 TeV and CDF Run-2 data especially pull toward smaller  $\alpha_s(M_Z)$  values, compared to the preference of DØ and ATLAS for a somewhat larger  $\alpha_s(M_Z)$ . This produces a much lower central value

$$\alpha_s(M_Z) = 0.1099 \pm 0.0062 \quad (68\% \text{ C.L.}), \quad (3.4)$$

that is well below the world average, with a larger uncertainty.

In summary, the comparison between the two different treatments for the correlated systematic uncertainties in inclusive jet production, `ksys=1` and `ksys=2`, demonstrates that these measurements are particularly sensitive to the choice of treatment. As we emphasized, requiring all correlated errors to be normalized according to the `ksys=2` (additive) choice may exaggerate the downward pull on  $\alpha_s(M_Z)$  and in fact introduce a statistical bias. An analogous downward shift has been noted in the NNPDF precision determination [24] of  $\alpha_s(M_Z)$ . Its final  $\alpha_s(M_Z)$  is quoted for the additive prescription (the analog of our `ksys=2`). Given that the additive vs. multiplicative nature of the provided correlated errors is largely undisclosed, and other treatments may involve biases as well, this exercise shows that details of the systematic error models play the central yet understated role in the extraction of  $\alpha_s(M_Z)$ .

#### IV. TOLERANCES AND DATA CLUSTERING SAFETY

One of the conclusions from Sec. III.2 is that, regardless of the implementation of the experimental correlation models, we observe a large spread among the most preferred  $\alpha_s(M_Z)$  among the different classes of experiments (DIS, DY, and Jet and top-quark pair production (Jet+ $t\bar{t}$ ) combined), as quantified by the positions of the minima of their  $\chi^2$  profiles in Fig. 4. If the errors are quantified by the  $\Delta\chi^2 = 1$  criterion, leading to  $\delta_{68\%}\alpha_s(M_Z) \sim 0.0004$ , the discrepancies among the preferred  $\alpha_s(M_Z)$  values from different classes of processes are truly significant. In particular, we noticed that the DIS measurements show a large disagreement with DY and Jet+ $t\bar{t}$  measurements. This behavior reveals the presence of tensions between the experiments within the CT25 global data set, which can also be established by other means.

Even when theory perfectly agrees with data, the  $\chi_E^2/N_{\text{pt}}$  ratios of individual experiments fluctuate around the expectation of one with a known probability. What is actually seen in all global fits is that the spread of  $\chi_E^2/N_{\text{pt}}$  is wider than this normal distribution arising from purely stochastic fluctuations. One can demonstrate this enlargement of discrepancies by considering histograms of effective Gaussian variables  $S_E$  [25] constructed from  $\chi_E^2$ . While, in the absence of tensions, the distribution of  $S_E$  is expected to be consistent with the standard normal distribution  $\mathcal{N}(0, 1)$ , the empirically obtained histograms of

$S_E$  for the CT, MSHT, and NNPDF global fits are wider than  $\mathcal{N}(0, 1)$ . This behavior raises the question of finding consistent procedures to combine the  $\alpha_s(M_Z)$  values from individual experiments and their corresponding uncertainties.

We mentioned that the naive application of the  $\Delta\chi^2 = 1$  criterion to the total  $\chi^2$  in the CT25 fit would result in  $\alpha_s(M_Z) = 0.1184 \pm 0.0004$ , which is smaller than the uncertainty of the world average quoted in the PDG [61]. In this and next section, we will review several strategies to obtain more realistic error estimates:

1. Introducing tolerance on the PDF errors in Sec. IV.1; exploration of data clustering safety of such prescriptions in Sec. IV.3;
2. Reclustering of data sets in Sec. IV.4;
3. Bayesian model averaging and data reweighting in Sec. V.

These are just some possible techniques, which nevertheless give a sense of what modifications to the  $\Delta\chi^2 = 1$  prescription one might expect with the realistic data in the PDF fit.

#### IV.1. Global and Dynamical Tolerance Criteria

Tolerance-based methods aim to account for fit imperfections such as tensions by modifying the  $\Delta\chi^2 = 1$  criterion assigning an increase in  $\chi^2$  to the 68% CL uncertainty. The simplest global tolerance [68] uniformly associates the 68% CL uncertainty with an increase  $\Delta\chi^2 = T^2 > 1$  for any combination of PDF parameters. This prescription may be too crude, as e.g. tensions among experiments are likely to constrain different combinations of PDF parameters in unsimilar ways. The dynamic tolerance leverages constraints from individual experiments to obtain  $T^2$  values independently for each orthogonal direction in the PDF parameter space in the Hessian formalism.

**Global Tolerance.** A common way to introduce either the global or dynamic tolerance is to consider quantiles of the probability density  $P(x)$  supported on  $-\infty < x < \infty$ . The quantile  $\xi(P, v)$  at cumulative probability  $v$  is defined by

$$\int_{-\infty}^{\xi(v)} P(x)dx = v. \quad (4.1)$$

To define the global tolerance (GT) at the 68% CL (corresponding to  $v = 0.68$ ) for  $\alpha_s(M_Z)$ , one might consider  $P(x)$  for the  $\chi^2$  distribution of the whole data set. Then, one determines  $T^2$ , or equivalently constructs the 68% CL interval  $\alpha_{s,\min} \leq \alpha_s(M_Z) \leq \alpha_{s,\max}$ , from the quantile  $\xi(\chi^2(N_{\text{pt}}), 0.68)$  of the  $\chi^2$  distribution with  $N_{\text{pt}}$  degrees of freedom.

The CT [39, 69] and MSHT [70] groups implement variations of this generic procedure in part to account for the more-than-normal excess of the best-fit  $\chi_0^2$  above its expectation value  $N_{\text{pt}}$ . For the purpose of this discussion, we will approximate both the CT and MSHT procedures by the following simplified prescription based on the effective Gaussian variable  $S$ .

$S$  represents a linearized  $Z$  score, i.e., it is a function of  $\chi^2$  that is distributed approximately according to  $\mathcal{N}(0, 1)$  and is easier to work with than the  $\chi^2$  distribution with  $N_{\text{pt}}$  degrees of freedom. For each  $\chi^2$ , the corresponding  $S(\chi^2, N_{\text{pt}})$  can be computed using either a simpler Fisher's approximation [71],

$$S(\chi^2, N_{\text{pt}}) = \sqrt{2\chi^2(N_{\text{pt}})} - \sqrt{2N_{\text{pt}} - 1}, \quad (4.2)$$

or a more precise formula by T. Lewis [72],

$$S(\chi^2, N_{\text{pt}}) = \left( -1 + \frac{1}{9N_{\text{pt}}} + \frac{1}{1 - \frac{1}{6} \ln\left(\frac{\chi^2}{N_{\text{pt}}}\right)} \right) \frac{\sqrt{18N_{\text{pt}}}}{1 + \frac{1}{18N_{\text{pt}}}}. \quad (4.3)$$

For both the CT and MSHT tolerance implementations, which are fully specified in their respective articles, the following mapping holds for the credibility interval up to subleading terms in  $1/N_{\text{pt}}$ :

$$\alpha_{s,\text{min}} \leq \alpha_s \leq \alpha_{s,\text{max}} \Leftrightarrow S(\chi^2(\alpha_s), N_{\text{pt}}) \leq S(\chi_0^2, N_{\text{pt}}) + \xi(\mathcal{N}(0, 1), v). \quad (4.4)$$

That is, the uncertainty interval at probability  $v$  is found by selecting those  $\alpha_s$  values for which the Gaussian variable  $S(\chi^2(\alpha_s), N_{\text{pt}})$  does not exceed its value  $S(\chi_0^2, N_{\text{pt}})$  at the global minimum by more than the quantile  $\xi(\mathcal{N}(0, 1), v)$  determined from  $\mathcal{N}(0, 1)$ .

The prescription (4.4) simplifies the calculation of the probability intervals, while being numerically close to the CT and MSHT full implementations. To compute uncertainties at 68% and 90% CL, one takes  $\xi(\mathcal{N}(0, 1), 0.68) = 0.468$  and  $\xi(\mathcal{N}(0, 1), 0.90) = 1.28$ .

**Dynamical Tolerance.** When the quantiles in Eq.(4.1) are computed for each  $\chi_E^2$  profile of the individual data sets, and then a single uncertainty range is constructed from their combination, we refer to it as the “dynamical tolerance uncertainty” [25, 70]. Suppose the global tolerance (GT) applied just to experiment  $E$  renders the uncertainty range  $\alpha_{s,\text{min}}^{(E)} \leq \alpha_s(M_Z) \leq \alpha_{s,\text{max}}^{(E)}$ . The dynamic tolerance (DT) interval for the full data set is constructed separately from the upper and lower boundaries for each experiment as

$$\alpha_{s,\text{min}}^{\text{DT}} \equiv \max_E \alpha_{s,\text{min}}^{(E)}, \quad \alpha_{s,\text{max}}^{\text{DT}} \equiv \min_E \alpha_{s,\text{max}}^{(E)}. \quad (4.5)$$

**The two-tier CT18 uncertainty.** The global and dynamical tolerance can be combined into a more complex constraint, such as the two-tier tolerance prescription used by CT10, CT14, and CT18 PDFs. In this prescription, the global tolerance with  $T^2 \sim 37$  is combined with the “tier-2” dynamical tolerance at

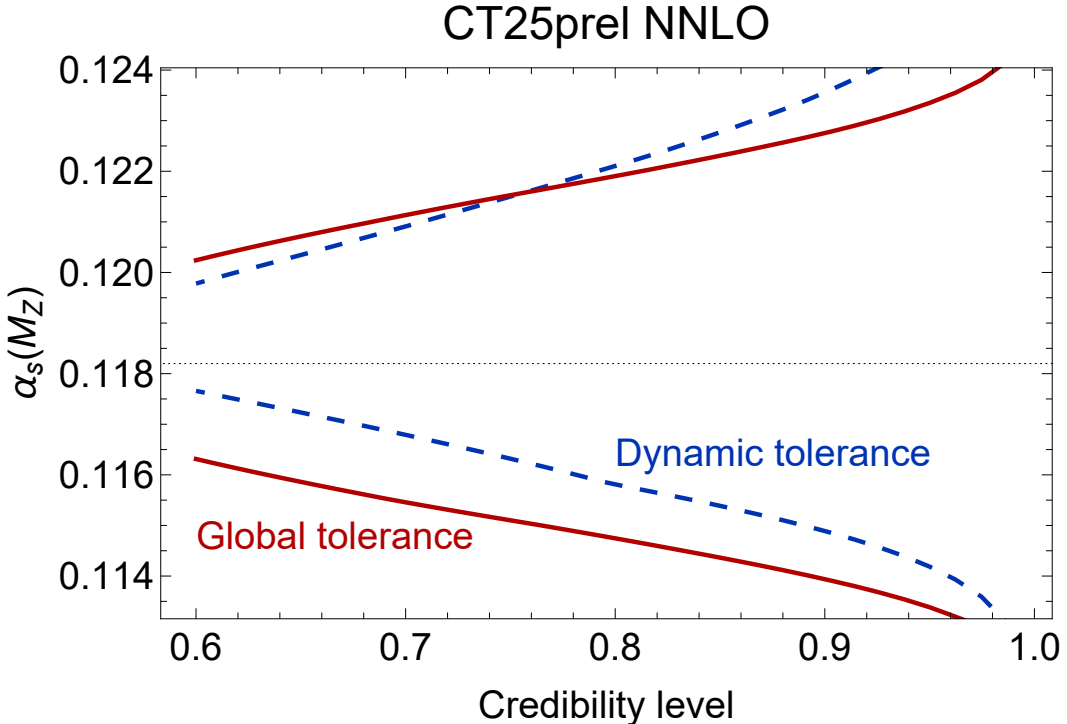


FIG. 6.  $\alpha_s(M_Z)$  uncertainties in the CT25 NNLO fit as a function of the credibility level for the global and dynamical tolerance criteria. The DT error band is computed using 49 published data sets of the CT25 baseline.

the 68% CL. The goal is of the current study is to bypass this definition, which otherwise would require, in particular, to estimate the global  $T^2$  through the quantile argument or by another means. The dynamic tolerance, on the other hand, depends on how the data are partitioned into “experiments”. Different partitions modify the DT uncertainties, which leads to the concept of “data clustering safety” that we will soon discuss.

#### IV.2. Properties of the dynamic tolerance

The dynamical tolerance (DT) proved to be convenient when accounting for constraints from individual experiments on PDF uncertainties. That said, at the detailed level, the DT behaves more elaborately than the GT. These peculiarities come to the forefront when one strives to elevate its precision.

**DT uncertainties neglect correlations among the data sets via the shared PDF parameters.** The correlations are considered when obtaining the central prediction and neglected when estimating the uncertainty. Indeed, the global minimum that defines the central prediction arises from the correlated constraints imposed by all experiments on the PDFs. When computing the quantiles of experiments, these correlations are neglected – this approximation breaks at some level.

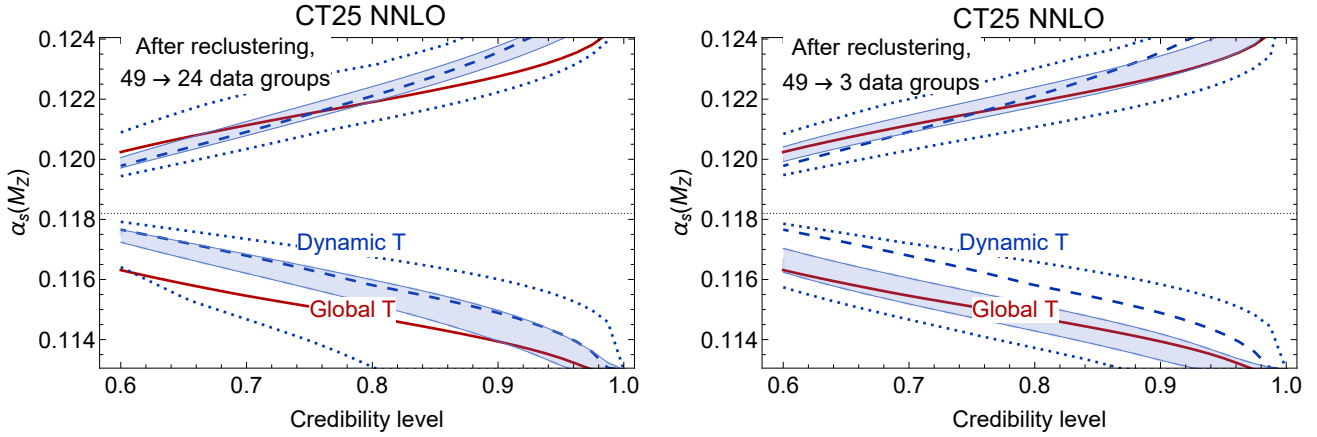


FIG. 7. Dependence on the dynamic tolerance uncertainties on the clustering of experiments in the CT25 NNLO fit. The red solid and blue dashed curves indicate the same GT and DT uncertainties as in Fig. 6. On the top we superimpose DT uncertainties from 10000 alternative clusterings of experiments in which the 49 original data sets were randomly combined in 24 clusters (left) and 3 clusters (right). At each credibility level, 6800 instances of the revised DT uncertainties fall within the light-blue bands. Blue dotted lines indicate the most extreme DT uncertainties among the 10000 instances. On average, the span of the DT errors reduces with more clusters and approaches the GT error with fewer clusters.

**DT intervals tend to be asymmetric** around the central value given by the position of the global minimum for all experiments. This can be explicitly seen from Eqs. (4.4) and (4.5), showing that the DT intervals are determined from *changes* in the probabilities of two most constraining experiments  $E$  with respect to the global  $\chi^2$  minimum.<sup>4</sup> For example, Fig. 6 compares the GT and DT uncertainties in the CT25 NNLO fit for credibility levels indicated on the horizontal axis. In this case, the GT is found from the quantile of the baseline data set. The DT is constructed from the quantiles of 49 contributing data sets and has obvious asymmetry above and below the central  $\alpha_s(M_Z)$ .

**DT is sensitive to clustering of data.** It depends on what counts as an independent experiment. Usually, one constructs the DT it from the  $\chi^2$ 's of the published data sets. It could be equally constructed from some other clusters of data, e.g., by combining (clustering) the published data sets into “supersets” or dividing them into “subsets”.

Figure 7 shows the same default GT and DT uncertainties for the 49 data sets as in Fig. 6. In addition, we recomputed the DT 10000 times, every time randomly combining the 49 data sets into 24 clusters in the left subfigure and into 3 clusters in the right one. For every CL value, we thus quantify the uncertainty on the DT uncertainty, communicated in the figure by filled blue bands containing 6800 instances of the reclustered DT intervals, as well as the dotted blue bands indicating the most extreme

<sup>4</sup> In the complete the CT or MSHT implementations of the DT formulas, such behavior is achieved by applying the quantile to the ratio  $S(\chi_E^2)/S(\chi_{E,0}^2)$  or  $\chi_E^2/\chi_{E,0}^2$ , not to  $S(\chi_E^2)$  or  $\chi_E^2$  itself.

instances among the 10000 reclustered DT intervals. From Fig. 7, it is clear that the average length and uncertainty of the DT interval depend on reclustering. Fewer clusters bring the DT uncertainty closer to the GT uncertainty, corresponding in this example to a single global data cluster. Conversely, finer clustering reduces the DT uncertainty interval.

Furthermore, we expect that clustering a pair of inconsistent experiments increases the DT interval. Conversely, splitting an inconsistent experiment into two or more clusters may reduce the DT interval. The reason is that the DT measures the change in the  $\chi_E^2$  compared to its value at the best fit. When an experiment  $E$  is in a disagreement, the change in its  $\chi_E^2$  is steep and often nonlinear. When inconsistent experiments are combined, their combined change may be much slower than for each one individually, resulting in a larger DT error. On the other hand, an internal inconsistency of a data set may be obviated by dividing this data set into incompatible parts, which may reduce the DT error.

Figure 8 summarizes this behavior by showing the DT uncertainty at 68% CL and 90% CL for the CT25prel baseline data comprised of 52 published data sets. In addition to the GT uncertainty, corresponding to one cluster containing all data, we show the DT uncertainty for 52 published data sets, as well as for alternative clusters detailed in Sec. IV.4.

The figure makes it obvious that the DT uncertainty changes depending on the clustering procedure. When data are split into a large number of clusters (1000 in Fig. 8), the DT uncertainty can be essentially zero, as it becomes very likely that a few outlier data points somewhere in the data sample will lead to a very tight DT constraint on  $\alpha_s(M_Z)$ .

### IV.3. Data clustering safety of uncertainty estimates

The previous subsection points out that the DT uncertainty depends on how the data are clustered. The fitting groups are constructing the DT using the full published data sets as independent clusters, but other reasonable clustering choices are obviously possible, often leading to different DT intervals.

Such sensitivity would raise concern that the DT uncertainty estimate on a fundamental parameter is *unsafe* at some level with respect to the user-chosen data clustering prescription. In contrast, the GT is trivially clustering-safe.

The key point here is that reclustering of the data sets modifies the degree of tensions present in the data. For instance, in a version of the CT25prel fit to 52 data sets shown in Fig. 8, the GT estimate is  $\alpha_s(M_Z) = 0.1179 \pm 0.0024$ , i.e. the error is practically symmetric. The default DT error is  $0.1179^{+0.0024}_{-0.0011}$ , showing a pronounced asymmetry. Upon reorganizing the data sets into 3 clusters, without breaking the data sets, in some cases the data sets are grouped so that their opposite pulls on  $\alpha_s(M_Z)$ , and in other cases these pulls are maximally exacerbated. When the tensions are largely cancelled, the 3-cluster DT

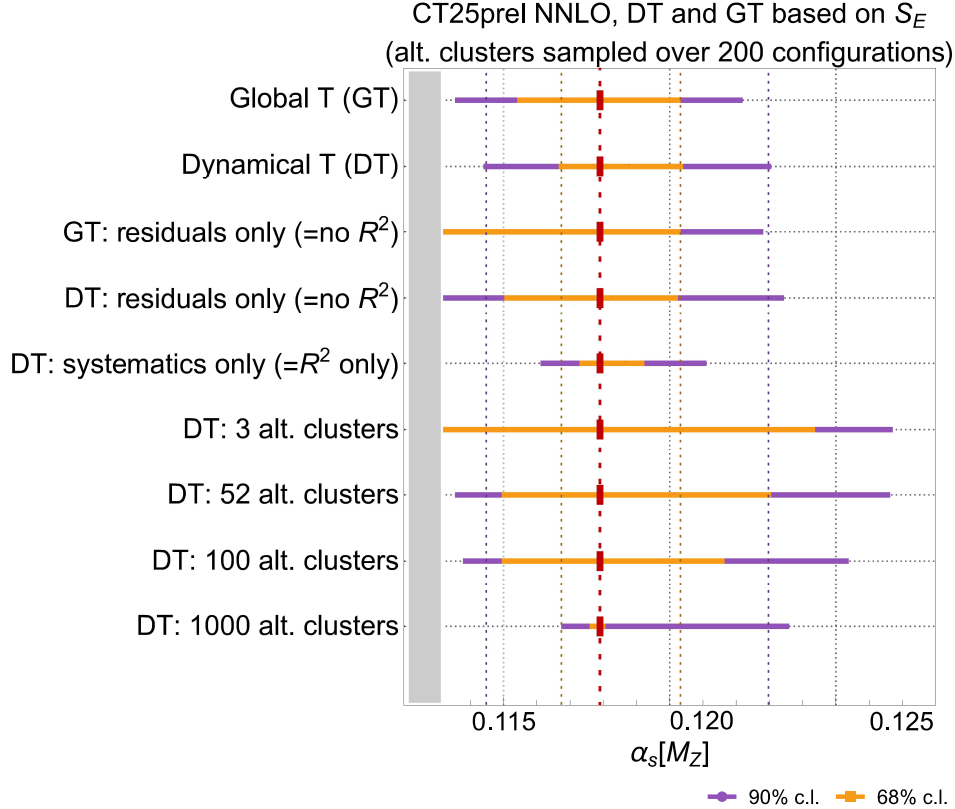


FIG. 8. Global and dynamical tolerance uncertainties on  $\alpha_s(M_Z)$  at the 68% and 90% CL for various clustering procedures applied to the CT25prel baseline. DT uncertainties are estimated according to the default prescription, without and with including the sum  $R^2$  of best-fit nuisance parameters, and optionally by reclustering the data into 3, 52, 100, and 1000 clusters as explained in Sec. IV.4. For the reclustered data, the DT errors are averaged over 200 alternative configurations.

error becomes nearly symmetric and larger than the GT one, e.g.,  $0.1179^{+0.0032}_{-0.0028}$ . When the clustering magnifies the tensions, the 3-cluster DT errors vary more and can be highly asymmetric or not, for instance,  $0.1179^{+0.0021}_{-0.0008}$  or  $0.1179^{+0.0016}_{-0.0019}$ .

The DT estimates thus in principle should be supplemented by additional tests of the degree of their clustering (un)safety. In light of what was said above, the DT errors for the  $\alpha_s$  determination vary between zero and the GT errors. One could take an envelope of these DT errors as a conservative estimate, or an average DT error over many clustering configurations as an optimal estimate. In our specific case, the latter estimate is close to the default one, and hence the final uncertainty combination will concentrate on the default DT tolerance.

#### IV.4. Data reclustering and $K$ -folding

In the remainder of this section, we will summarize the procedure employed to divide the published data sets into many clusters illustrated in Fig. 8. At the end, we will comment on the potential impact of cross validation procedures in the Monte-Carlo-based approaches on the  $\alpha_s$  uncertainty estimate.

##### IV.4.1. Reclustering algorithm

Reclustering is based on the representation of the best-fit  $\chi^2$  in Eq. (2.4) by the quadrature sums  $D^2$  and  $R^2$  of data residuals  $r_{0,k}^{(E)}$  and nuisance parameters  $\lambda_{0,\alpha}^{(E)}$ . If we neglect correlations via the PDF parameters, as was done to justify the DT to start with, then  $[r_{0,k}^{(E)}]^2$  and  $[\lambda_{0,\alpha}^{(E)}]^2$  from all data sets can be separately and independently collected (“shuffled”) into alternative clusters of data points, and then the DT can be formed from such clusters.

To examine how the DT bands change when we partition the published data sets instead of combining them, we implement the following exercise. We work with the CT25prel baseline, create a grid of  $N_{\alpha_s} = 21$  values of  $\alpha_s(M_Z)$  between 0.113 and 0.129, and select a reference  $\alpha_s(M_Z)_{\text{ref}}$ , which in this case we set equal to the best-fit  $\alpha_s(M_Z) = 0.1179$ . For each  $\alpha_s$ , we can organize all  $\chi_R^2$  components in Eq. (2.4) into two vectors  $\vec{v}_r$  and  $\vec{v}_\lambda$  as

$$\vec{v}_r = \left\{ r_{0,1}^{(1)}, \dots, r_{0,N_{\text{pt}}^{(1)}}^{(1)}, \dots, r_{0,1}^{(N_E)}, \dots, r_{0,N_{\text{pt}}^{(N_E)}}^{(N_E)} \right\}, \quad (4.6)$$

$$\vec{v}_\lambda = \left\{ \lambda_{0,1}^{(1)}, \dots, \lambda_{0,N_\lambda^{(1)}}^{(1)}, \dots, \lambda_{0,1}^{(N_E)}, \dots, \lambda_{0,N_\lambda^{(N_E)}}^{(N_E)} \right\}, \quad (4.7)$$

$$\text{so that } \chi_R^2 = D^2 + R^2, \quad D^2 \equiv \|\vec{v}_r\|^2, \quad R^2 \equiv \|\vec{v}_\lambda\|^2. \quad (4.8)$$

Focusing first on reclustering of  $D^2$  into  $N_{cl}$  clusters with equal numbers of data points (modulo  $N_{cl}$ ), we randomly assign the  $\vec{v}_r$  components into these clusters using a random generator engine (e.g., Mersenne-Twister [73]). We keep the same assignment of the residuals into clusters for all  $\alpha_s(M_Z)$  values on the grid. The  $\chi_E^2$  dependence on  $\alpha_s(M_Z)$  for the  $N_{cl}$  pseudoexperiments now defines the DT uncertainty on  $\alpha_s(M_Z)$ . To construct the DT, we follow the same procedure as for the published data sets in Sec. IV.1. Namely, for each cluster  $E$  we compute the quantiles at our CL, determine  $\alpha_{s,\min}^{(E)}$  and  $\alpha_{s,\max}^{(E)}$  for this quantile, and then construct the DT bounds as in Eq. (4.5), where  $E$  now runs over the clusters.

For every  $N_{cl}$ , we repeat this procedure many (e.g.,  $> 200$ ) times, each time reshuffling the assignment of  $r_{0,k}^{(E)}$ . Since the best-fit residuals and nuisance parameters enter  $\chi_R^2$  as independent degrees-of-freedom, we can analogously shuffle the nuisance parameters from  $R^2$  into random clusters; or, since the contri-

butions from  $R^2$  can only strengthen the DT uncertainties based solely on the residuals, we can initially omit  $R^2$  for simplicity.

#### IV.4.2. Separate reclustering of residuals and nuisance parameters

We illustrate the possibility of separate reclustering of the residuals and nuisance parameters by two figures. Figure 9 goes back to the example of the GT and DT uncertainties for the published data sets in Fig. 6 for the CT25 baseline and now shows the DT uncertainties constructed only with  $D^2$  and only with  $R^2$  for the CT25prel baseline.<sup>5</sup> The role of  $R^2$  appears to be somewhat different for the GT and DT cases. In the GT case, the  $R^2$  has a more constraining power on the uncertainty: if it were to be the only metric for the uncertainty, we would obtain a very small error (red dashed band). Conversely, without the  $R^2$  contribution, the GT error (red solid lines in Fig. 9) are significantly wider than the GT error based on both residuals and nuisance parameters, or  $D^2 + R^2$ , in Fig. 6. However,  $R^2$  is in general not perfectly determined, due to lack of full control on the correlated systematic uncertainties.

In the case of the DT, however, the errors without  $R^2$  (blue dashed lines in Fig. 9) largely follow those based on  $D^2 + R^2$  in Fig. 6. In other words, the residuals appear to play a more important role in the DT case.

Figure 8 showed how the 68% and 90% CL error estimates change when we vary the DT clustering procedure. Figure 10 extends this comparison to show error estimates for other credibility levels, including the residuals only (that is, neglecting  $R^2$ ). In this figure, the ‘‘Global T: no  $R^2$ ’’ and ‘‘Dynamical T: no  $R^2$ ’’ refer to the GT and DT uncertainties based on the full baseline. The ‘‘52 alt. clusters’’ and other lines refer to randomly generated clusters constructed by reshuffling the residuals in the 52 experimental data sets of CT25prel. For the alternative clusters, the lines show the envelopes of the DT estimates for 200 shuffles of the corresponding alternative clusters.

In an ideal scenario, in the absence of tensions among the data, alternative cluster configurations would produce approximately the same estimate for the  $\alpha_s(M_Z)$  uncertainty. In reality, when we partition into a lot of clusters, taking the outcome of the DT without  $R^2$  by itself may already produce a stringent (likely, too stringent) uncertainty on  $\alpha_s(M_Z)$ . However, the constraints may be weaker for other cluster configurations, and including  $R^2$  into clustering may additionally reduce or increase the strength of the DT constraints by modifying the tensions, similarly to what we saw for the DT that reclustered the published data sets.

---

<sup>5</sup> These uncertainties do not change much between the two baselines. In this and following figure, the lower bands saturate at  $\alpha_s(M_Z) = 0.113$ , the lowest point on our  $\alpha_s$  grid.

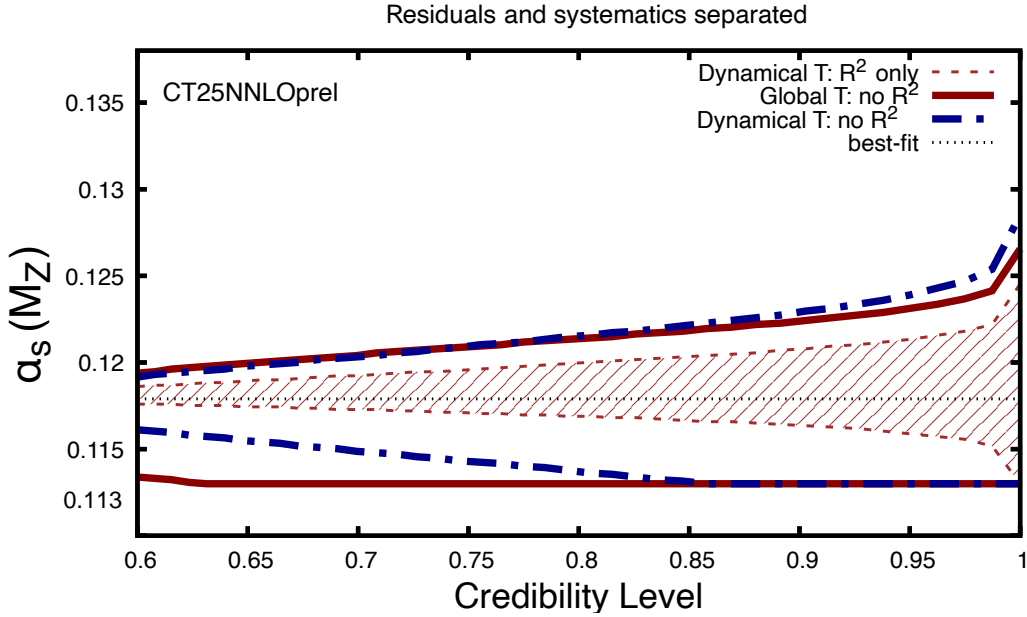


FIG. 9. Contributions to the GT and DT uncertainties vs. the credibility level for the CT25prel baseline from nuisance parameters ( $R^2$ ) only and from residuals ( $D^2$ ) without  $R^2$ .

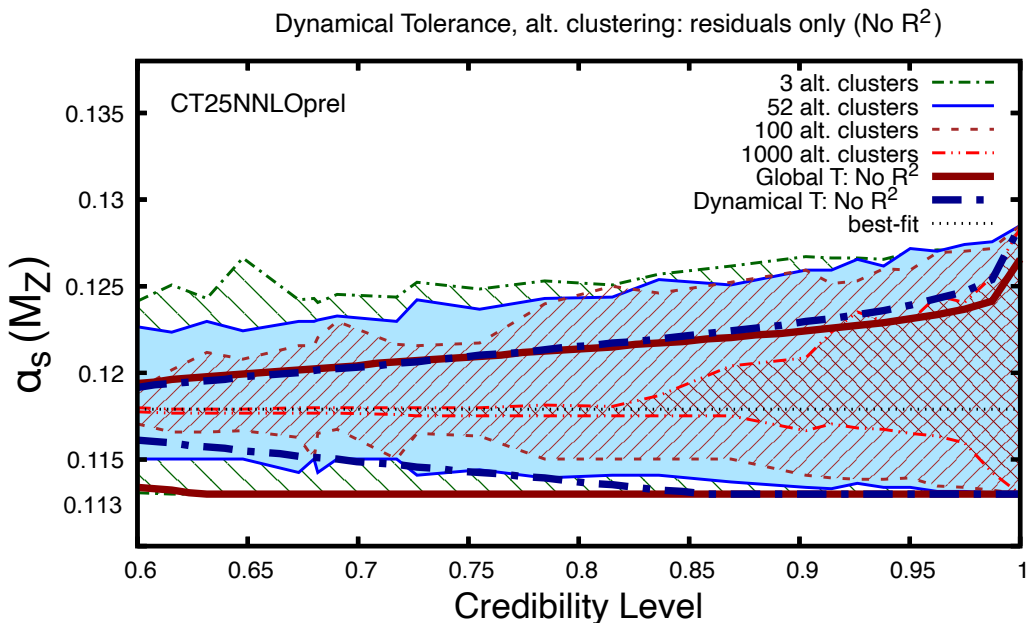


FIG. 10. Reclustering without  $R^2$ :  $\alpha_s(M_Z)$  as a function of the credibility level for the dynamical and global tolerance criteria compared to different alternative cluster configurations.

#### IV.4.3. $K$ -folding impact on $\alpha_s$

In our next example, we will explore how the uncertainties on  $\alpha_s(M_Z)$  obtained in MC/ML approaches may be affected by common cross validation techniques that partition the baseline data set into training, testing, and occasionally validating components. An example of such procedure is  $K$ -folding [74, 75] introduced in the NNPDF determination [24] of  $\alpha_s(M_Z)$  to mitigate overfitting of the neural-network model for PDFs. Since  $K$ -folding involves reclustering of the baseline data and may be sensitive to data tensions, we will briefly review its possible impacts on the  $\alpha_s(M_Z)$  uncertainty.

In the common  $K$ -folding procedure, each replica of the data baseline is partitioned into several folds (clusters), with one fold set aside as the test data set. The model is then trained on the union of remaining folds. A figure of merit called “loss function”  $L$  is optimized so as to achieve good agreement with both the training and testing sets. The training procedure is iterated by excluding every fold in turn and training on the rest of the folds. In the  $\alpha_s$  study, each iteration of such training+cross validation also returns the best-fit  $\alpha_s(M_Z)$  and its uncertainty. The final  $\alpha_s(M_Z)$  is determined by weighted averaging over all replicas and  $K$ -folding iterations. The weights may be given in terms of the respective  $\alpha_s$  uncertainties from the iterations.

Based on our preceding discussion, we expect the outcome of  $K$ -folding for  $\alpha_s$  determination from the global data set to vary depending on the clustering algorithm and uncertainty definition. In the NNPDF study, each replica of the published data sets is partitioned into the training set and testing fold as 3:1, without breaking the data sets apart. The  $\alpha_s$  uncertainty from each iteration of training is determined essentially according to the  $\Delta\chi^2 = 1$  criterion. The final  $\alpha_s(M_Z)$  is obtained by averaging over the data replicas and  $K$ -folding iterations using  $1/(\Delta\alpha_s(M_Z))^2$  from each iteration as the weight. Their resulting value  $\alpha_s(M_Z) = 0.1194^{+0.0007}_{-0.0014}$ . We pointed out in Sec. III.2 that the NNPDF central value changes depending on the normalization for the experimental systematic errors, in accord with our own findings. The NNPDF uncertainties are generally smaller than ours. While reproducing them is beyond the scope

	cluster 0	cluster 1	cluster 2	cluster 3
$N_{\text{pt}}$	1113	1113	1112	1112
$\chi^2_R$ (no $R^2$ )				
shuffle 1	1094	1157	1281	1177
shuffle 2	1102	1158	1252	1198
shuffle 3	1065	1239	1251	1156

TABLE II. Numbers of points and  $\chi^2_R$  (without the systematic contribution  $R^2$ ) for three random combinations (shuffles) of the residuals into four pseudodata clusters.

of our study, we can elucidate the variability of the preferred central values and their uncertainty under different clustering methods using the following simplified exercise.

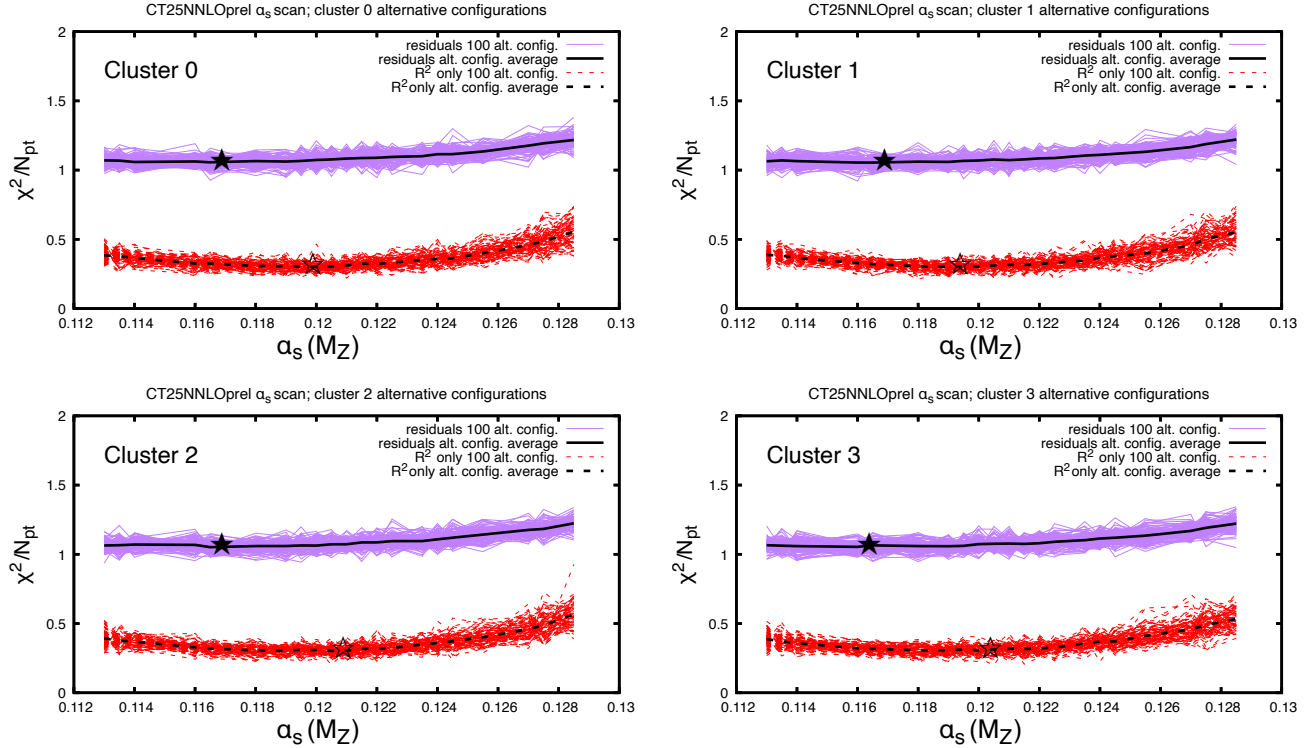


FIG. 11.  $\chi^2/N_{\text{pt}}$  as a function of  $\alpha_s(M_Z)$  for 100 alternative configurations of residuals and nuisance parameters partitioned into four equal-sized clusters.

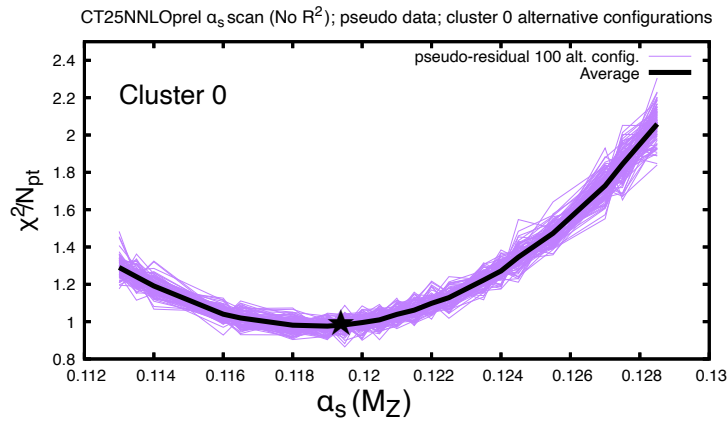


FIG. 12.  $\chi^2/N_{\text{pt}}$  as a function of  $\alpha_s(M_Z)$  for cluster 0 with random reshuffling of pseudoresiduals from pseudodata without tensions.

In contrast to the full  $K$ -folding procedure, we will not refit (optimize) the PDFs for each data partition, which would be too computationally expensive. Instead, we will examine uncertainties by

reclustering the output of the CT25prel global fit, similarly to what was done in the previous sections. In addition, to assess their independent impact, we will separately consider the residual and nuisance-parameter contributions.

**Dependence of the central  $\alpha_s(M_Z)$  on clustering.** We generate multiple shuffles of the residuals into four clusters, with about 1113 points in each cluster, as outlined in Sec. IV.4.1. Table II reports the numbers of points and  $\chi^2$  contributions for three representative shuffles in our series. Similarly, we can construct four “ $R^2$ ” clusters consisting of the shuffled best-fit nuisance parameters. Figure 11 illustrates the outcome of one such exercise, in which 100 instances of four clusters were generated. The figure separately depicts the individual  $\chi^2/N_{pt}$  ratios for the residuals (purple lines) and nuisance-parameter (red-dashed lines). Each purple (red) line corresponds to a different shuffle configuration. The black lines represent the  $\chi^2/N_{pt}$  average values. The stars represent the minima of the average curves which indicate the  $\alpha_s(M_Z)$  central-value preference. No tolerance criterion is applied here; we simply calculate the  $\chi^2/N_{pt}$  in each cluster for many different random alternative configurations and varied  $\alpha_s(M_Z)$ .

One goal of this exercise is to determine whether the random fluctuations due to the reshuffling process are compatible with their  $\mathcal{N}(0, 1)$  distribution expected when the data sets mutually agree. The  $\chi^2/N_{pt}$  vs.  $\alpha_s(M_Z)$  for the latter case is shown in Fig. 12, for which we generated an ensemble of the “cluster 0” configurations from pseudoresiduals that were generated according to  $\mathcal{N}(0, 1)$  from a baseline pseudodata without tensions and assuming the “truth”  $\alpha_s(M_Z) = 0.119$ .

It is therefore interesting to confront the idealized pseudoresidual scenario against the realistic distributions of the residual and  $R^2$  clusters. In the ideal case in Fig. 12, the clusters follow a deep parabola centered at the “truth”  $\alpha_s(M_Z)$ . In the real case in Fig. 11, all clusters have shallower dependence on  $\alpha_s(M_Z)$ . The parabolic behavior is particularly wide for the residuals and slightly narrower for the nuisance parameters. The clusters of the real residuals all prefer an approximately stable value of  $\alpha_s(M_Z) \approx 0.1165$ . The preferred  $\alpha_s(M_Z)$  of the  $R^2$  clusters varies more, between 0.119 and 0.121 depending on the cluster. We read off these values from the central curves of each cluster, obtained by averaging the  $\chi^2/N_{pt}$  curves over many alternative configurations. The fluctuations around these curves, however, are roughly of the same magnitude as in the idealized case of Fig. 12. These observations suggest that tensions among the data sets primarily flatten the  $\chi^2/N_{pt}$  curves relatively to the no-tension scenario. They also introduce variability in the preferred values of  $\alpha_s(M_Z)$  for the  $R^2$  clusters, as different groups of experimental systematic uncertainties exert substantial and inconsistent pulls on  $\alpha_s(M_Z)$ .

**$\alpha_s(M_Z)$  uncertainty in the four-cluster exercise.** Figure 11 demonstrates that the  $\chi^2/N_{pt}$  dependence of clusters is shallower than in the idealized case for which the  $\Delta\chi^2 = 1$  prescription is applicable.

Shuffle 1					
$\delta\alpha_s(M_Z) =$	$+0.00180$ $-0.00062$	$+0.00230$ $-0.00400$	$+0.00410$ $-0.00490$	$+0.00830$ $-0.00490$	
in 1-clusters:	{0}	{1}	{3}	{2}	
& 3-clusters:	{0,1,2}, {0,1,3}, {0,2,3}	{1,2,3}	N/A	N/A	
Shuffle 2					
$\delta\alpha_s(M_Z) =$	$+0.00102$ $-0.00038$	$+0.00507$ $-0.00490$	$+0.00515$ $-0.00490$	$+0.00943$ $-0.00490$	
in 1-clusters:	{0}	{1}	{3}	{2}	
& 3-clusters:	{0,1,2}, {0,1,3}, {0,2,3}	{1,2,3}	N/A	N/A	
Shuffle 3					
$\delta\alpha_s(M_Z) =$	$+0.00016$ $-0.00038$	$+0.00480$ $-0.00290$	$+0.00803$ $-0.00490$	$+0.00819$ $-0.00490$	
in 1-clusters:	{0}	{3}	{1}	{2}	
& 3-clusters:	{0,1,2}, {0,1,3}, {0,2,3}	{1,2,3}	N/A	N/A	

TABLE III. For each shuffle of the  $K$ -folding exercise, we report the  $\delta\alpha_s$  values found by applying the DT, as well as the one 1-cluster and three 3-clusters for which these  $\delta\alpha_s$  are achieved. The columns containing the  $\delta\alpha_s$  values and clusters are arranged so that the leftmost (rightmost) column contains the lowest (highest)  $\delta\alpha_s$ .

The question arises how to quantify the uncertainty in this situation. As was already stated, in an NNPDF-like approach, the  $\alpha_s$  uncertainties from individual iterations would affect the weights for the final  $\alpha_s$  averaging, and the final outcome would also reflect refitting the PDFs for each data partition into clusters, as well as averaging over partitions' sizes, which is beyond the scope of this study.

Just as one possibility, if the DT criterion is applied either to the “training set” consisting of 3 clusters or 1 “testing” cluster, it can render the uncertainty that can be substantially larger or smaller than the  $+0.0007$   
 $-0.0014$  from the NNPDF study. In its most granular realization, the DT criterion treats each residual as an independent “experiment”. Table III summarizes the outcome of applying such DT criterion to the three training clusters of the residuals (no  $R^2$ ) and to the one left out. Here we show the DT  $\alpha_s$  uncertainties for the same three shuffles as in Table II. These uncertainties can be either substantially smaller or larger than the NNPDF one, depending on the specific partition. The table also highlights the observation that, within a combination of any three clusters, the DT uncertainty of the whole cluster is equal to the smallest individual DT uncertainty among the constituent clusters. For this specific example, cluster 0 has the lowest  $\chi^2$  for the three shuffle configurations, cf. Table II. When combined with the other

two, this cluster drives the net uncertainty of the combination. For the fourth 3-cluster combination, the uncertainty is set by the second most precise individual cluster. According to the findings in Table III, the uncertainty on  $\alpha_s(M_Z)$  is not uniformly reproduced by each test cluster, and this is mainly ascribed to tensions in the data. The results do not change if we consider the average of the errors over a large number of shuffle configurations.

This exercise can in principle be applied to any number of clusters with  $N_{cl} \leq N_{pt}$  to explore the variability of  $\alpha_s(M_Z)$  and its uncertainty across the full granularity of data.

## V. BAYESIAN MODELS FOR UNCERTAINTY ESTIMATION

The fundamental assumption of the tolerance prescriptions is that all experiments agree on the parameter of interest in a certain region, and this region can be estimated from the augmented loglikelihood by following the described procedures. In contrast, Bayesian model averaging assumes that some experiments are more likely to be correct than the others and estimates the underlying probabilities for them to be correct from the data. In this section, we describe how two such models can be used to determine the best-fit  $\alpha_s$  and its uncertainty, working with the CT25 baseline data set as an example. As in the previous sections, we make a simplifying assumption that the correlations among the separate experimental data sets via the PDFs or other parameters are negligible, allowing us to treat these data sets as independent  $\alpha_s$  determinations in the good approximation.

### V.1. Bayesian Hierarchical Model

A Bayesian Hierarchical model (BHM) offers a method for combining  $\alpha_s(M_Z)$  determinations from the individual  $\chi_E^2$  of each experiment by following the procedure outlined in Ref. [76]. According to this model, one introduces a distribution of hyperpriors, from which one can draw possible values of the parameter of interest, in our case  $\alpha_s(M_Z)$ . Specifically, considering each  $\alpha_{s_i}(M_Z)$  to be the result of a random draw from a parent distribution, one can write

$$p(\alpha_{s_i}) = \int p(\alpha_{s_i}|\mu, \tau)p(\mu, \tau)d\mu d\tau, \quad (5.1)$$

where  $p(\mu, \tau)$  is a hyperprior distribution for the hyperparameters  $\mu$  and  $\tau$ . In Ref. [76] a  $\mu$ -independent hyperprior is proposed as follows:

$$p(\tau)d\tau^2 \propto \prod_{i=1}^N \left[ \frac{1}{\sigma_i^2 + \tau^2} \right]^{\frac{\beta}{2N}} d\tau^2, \quad (5.2)$$

where  $\beta$  is a parameter that determines the nature of the prior being used, and  $p(\tau)$  interpolates smoothly between a flat and a sharply peaked  $\tau$  distribution. If  $\beta = 0$ , one assumes a flat prior and hence a

larger spread of the hyperprior distribution. Therefore, small values of  $\beta$  are used for data sets that exhibit substantial disagreement, and vice-versa. We combine the data given in Table IV, according to which  $N = 3$  in Eq. (5.2) represents the number of  $\alpha_s(M_Z)$  measurements being combined and  $\sigma_i$  are the corresponding uncertainties. For  $\beta = 0$ , we find  $\alpha_s(M_Z) = 0.1181^{+0.0030}_{-0.0031}$ . The variation of the uncertainty estimate as a function of  $\beta$  is shown in Fig. 13 (left), where we note that the  $\alpha_s(M_Z)$  uncertainty reduces as  $\beta$  increases. Specifically, for  $\beta = 15$  we find  $\alpha_s(M_Z) = 0.1182^{+0.0006}_{-0.0007}$ . Given the large spread of  $\alpha_s(M_Z)$  values in Table IV and as suggested in Ref. [76], we use smaller values of  $\beta$ . Rather than choosing a single value of  $\beta$  we average over  $0 \leq \beta \leq 1$  which yields

$$\alpha_s(M_Z) = 0.1181^{+0.0022}_{-0.0023}. \quad (5.3)$$

In the next section, we repeat this exercise using a variant of the implementation of the hierarchical model, where the choice of the hyperparameters is determined through the use of statistical information criteria.

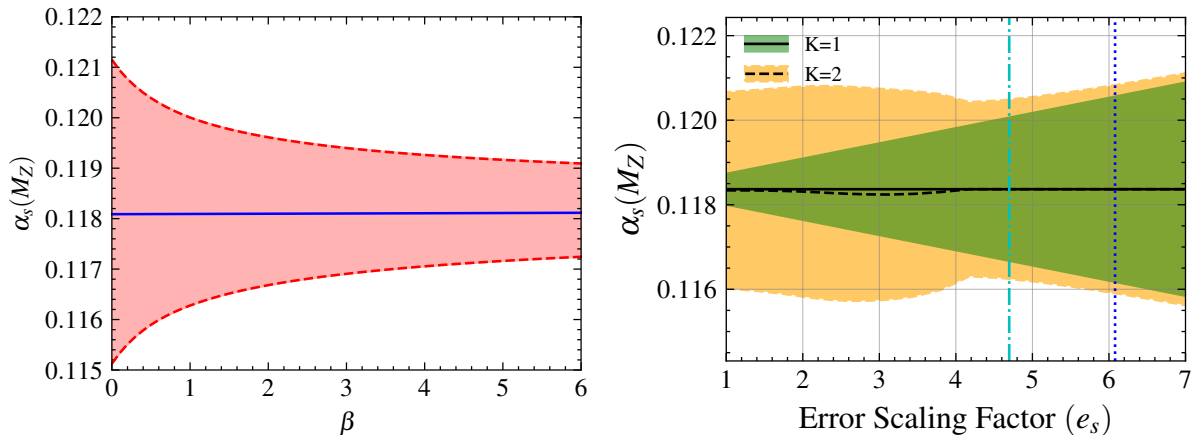


FIG. 13. Variation of the uncertainty on  $\alpha_s(M_Z)$  when using the BHM (left) with a hyperprior defined in Eq. (5.2), and when using the GMM (right) as a function of the error scaling factor  $e_s$ . The orange shaded region represents the uncertainty when setting  $K = 2$  in the GMM and the green shaded region represents the uncertainty for  $K = 1$ , which corresponds to the usual  $\chi^2$  fit. Also shown are vertical lines indicating the values of  $e_s \approx 4.7$  and  $e_s \approx 6.2$ , respectively corresponding to the values of the PDG scale factor and the value of the global tolerance  $T$ , that would give the same uncertainty estimate as the GMM. For both plots, the data used in the combination is shown in Table IV.

## V.2. Hierarchical Models via a Gaussian Mixture Model

In Ref. [77] a new Bayesian hierarchical model is proposed as a generalized likelihood, that is modeled via the Gaussian mixture model (GMM). In this section, we apply the GMM to the combination of the

three  $\alpha_s(M_Z)$  measurements in Table IV, with the aim of capturing the multi-modal feature of this data set with large spread.<sup>6</sup>

In the GMM,  $K$  Gaussian components are introduced so that the likelihood is modeled as

$$L(\alpha_s) = \sum_{k=1}^K w_k \mathcal{N}(\alpha_s | \mu_k, \sigma_k^2), \quad (5.4)$$

where  $w_k$  are mixture weights. The optimal value of  $K$  is determined using model selection criteria such as the Akaike Information Criteria (AIC) [78] and Bayesian Information Criteria (BIC) [79]. For the present combination, the choice of  $K = 2$  minimizes both the AIC and BIC. Note that  $K = 1$  corresponds to the standard  $\chi^2$  combination in Eq. (6.1). Minimizing the GMM log-likelihood yields a bimodal posterior for  $\alpha_s(M_Z)$ . Following the procedure of Ref. [77], we extract the  $\alpha_s(M_Z)$  central value and its uncertainty from this distribution, and find

$$\alpha_s = 0.1183 \pm 0.0023 \quad (\text{GMM, } K = 2). \quad (5.5)$$

We observe that, adopting a tolerance  $T$  such that  $\Delta\chi^2 = T^2 \simeq 33$  (equivalent to a scaling factor  $e_S \simeq 6.2$ , see Sec. VI.2 for the definition of the error scaling factor) produces an  $\alpha_s(M_Z)$  uncertainty from  $\Delta\chi^2$  that is comparable to that obtained via the GMM:

$$\alpha_s = 0.1183 \pm 0.0023 \quad (\text{scaled errors, } e_S \approx 6.24 \text{ or } T^2 \simeq 33).$$

In contrast, a scaling value of  $e_S \approx 6.9$  or equivalently,  $T^2 \approx 48.2$ , produces the same value of uncertainty estimate as produced by the global tolerance criterion given in Eq. (6.4).

Figure 13 (right) illustrates the dependence of the  $\alpha_s(M_Z)$  uncertainty on the error scaling factor  $e_S$  for both  $K = 1$  (standard  $\chi^2$ ) and  $K = 2$  (GMM). The solid- and dashed-black horizontal lines indicate the values of  $e_S$  defined above. The orange shaded region represents the uncertainty estimate using  $K = 2$ , whereas the green region represents the uncertainty for  $K = 1$ . When the errors are not rescaled, then  $e_S = 1$  and  $K = 1$  produces a very small uncertainty identical to the values presented in the last column of Table IV. On the other hand, the preferred model for  $e_S = 1$  corresponds to  $K = 2$ . An increase in the value of  $e_S$  corresponds to an increase in the uncertainty for  $K = 1$ , whereas the uncertainty for  $K = 2$  decreases at  $e_S \approx 3.5$ . This is the region where the AIC and BIC criteria start to exhibit a preference for the  $K = 1$  model, cf. Sec V.3. It is interesting to note that one could in principle use this fact to determine a value of  $e_S$  that reduces tension by an amount that makes the  $K = 1$  model preferable and in some sense making the data set more consistent. One could then use the uncertainty obtained in the  $K = 1$  case when  $e_S \approx 3.5$ , to determine the  $\alpha_s(M_Z)$  uncertainty. This choice however,

<sup>6</sup> A more complete implementation of the GMM requires modification of the  $\chi^2$  loss function, contributed from each experimental data set included in the fit, that we do not perform here.

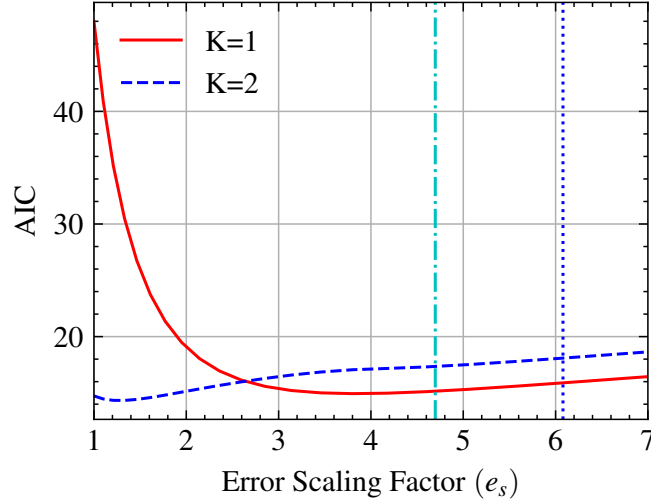


FIG. 14. Variation of the AIC with the error scaling factor  $e_s$  shown for both  $K = 1$  (red) and  $K = 2$  (blue) in the GMM. Also shown are the values of  $e_{SPDG} \approx 4.7$  (dot-dashed) and  $e_s \approx 6.2$  (dotted) which gives similar values of the uncertainty using the global tolerance criteria in Eq. 6.4.

produces poor fit with a large value of the reduced  $\chi^2$  as well as a very small uncertainty, we therefore do not use this approach here.

### V.3. Information Criteria and the GMM

We use the AIC to determine the optimal number of Gaussian mixtures  $K$  for the GMM. The AIC is defined as

$$\text{AIC} = N_p \ln N_{\text{pt}} - 2 \ln L(\bar{\alpha}_s) \quad (5.6)$$

where  $L(\bar{\alpha}_s)$  is the GMM likelihood given in Eq. 5.4 evaluated at the optimized value of  $\alpha_s$ ,  $N_{\text{pt}}$  is the number of data clusters and the number of independent parameters  $N_p$  for the GMM is given by

$$N_p = K \times N_{\text{parm}} + (K - 1) . \quad (5.7)$$

Since we profile the  $\chi^2$  over  $\alpha_s(M_Z)$ ,  $N_{\text{parm}} = 1$ . We vary the value of  $K$  from 1 through 5 and find that the value of  $K$  that minimizes the value of the AIC is  $K = 2$ . We further explore the impact of inflating uncertainties through the error scaling factor ( $e_s$ ) for two models: the usual  $\chi^2$  in Eq. 6.1, which corresponds to the choice  $K = 1$  in the GMM, and  $K = 2$ . The variation of AIC with  $e_s$  for these two models are shown in Fig. 14. Without rescaling the errors, i.e for  $e_s = 1$ , we find that the  $K = 1$  gives lower values of AIC and is therefore preferred. For this value of  $e_s$ , the  $K = 2$  model finds two possible values of  $\alpha_s(M_Z) = \{0.1154, 0.1193\}$ . As the value of  $e_s$  increases the data becomes more consistent, thus

increasing the value of AIC for  $K = 2$  and reducing the value of AIC for  $K = 1$ . Beyond the value of  $e_s \approx 2.3$ , the  $K = 1$  model becomes the preferred choice. For  $e_s \approx 2.3$ , the fit is still of poor quality with a large reduced  $\chi^2$ , hence we do not use this as a measure to set the value of  $e_s$ . For values of  $e_s \gtrsim 3.5$ , we see that the curves for AIC for both models increase linearly at the same rate. For these values of  $e_s$  the  $K = 2$  model does not find two numerically distinct values of  $\alpha_s(M_Z)$  and therefore begins to behave like the  $K = 1$  model, albeit some over-fitting due to the larger number of parameters. This also explains the kink like feature in Fig. 13 where there is a sudden reduction of the uncertainty for the  $K = 2$  model and the uncertainty for the  $K = 2$  model tracks the behavior of the  $K = 1$ . The slightly larger uncertainties for  $K = 2$  for  $e_s \gtrsim 3.5$  arise due to overfitting [77].

## VI. FINAL COMBINATION OF $\alpha_s$ DETERMINATIONS

Having reviewed the physics factors affecting the extraction of  $\alpha_s$  and several procedures to determine the  $\alpha_s$  uncertainty, we are ready to combine this information to provide the final  $\alpha_s$  determination.

In Sec. III.1 we pointed out that the  $\Delta\chi^2 = 1$  criterion would lead to an unrealistically small  $\alpha_s(M_Z)$  uncertainty, and that an additional  $\delta_{68\%}$  uncertainty must be associated to  $\chi^2_0$ . As a reminder, when examining the  $\chi^2$  profile for the CT25prel baseline Fig. 4, the application of the  $\Delta\chi^2 = 1$  criterion to the total  $\chi^2$  (black curve) would result in  $\alpha_s(M_Z) = 0.11837^{+0.00035}_{-0.00041}$ . This uncertainty is much smaller than the global average quoted in the PDG [61].

Moreover, in Sec. III.2, we analyzed the  $\chi^2$ -profile from different classes of experiments (DIS, DY, and Jet and top-quark pair production (Jet+ $t\bar{t}$ ) combined) and observed a significant spread in the minima of these profiles reflecting the presence of tension between the experiments. In particular, we noticed that the DIS measurements show significant disagreement with DY and Jet+ $t\bar{t}$  measurements. We also noted the sensitivity of the  $\chi^2$  profiles on only partly known normalizations of the correlated systematic errors controlled by the `ksys` parameter.

The limitation associated with a  $\Delta\chi^2 = 1$  criterion and the significant discrepancies observed in the preferred  $\alpha_s(M_Z)$  value by different experiments, raise the question of finding consistent procedures to combine the  $\alpha_s(M_Z)$  values and their corresponding uncertainties. We address this question in this section.

### VI.1. The central $\alpha_s$ value

In Sec. II, we observed that the choice between the acceptable baseline data sets affects the central  $\alpha_s$  value. The two described baselines, CT25prel and CT25, yield the central values of 0.1179 and 0.1185,

respectively. In the following, we will quote the latter as our final  $\alpha_s$  determination. In contrast, the choice between the baselines only weakly influences the uncertainty determination, which instead depends on the method for the estimation. In the following, we summarize the uncertainty ranges obtained with several such methods.

## VI.2. Uncertainty with the Particle Data Group prescription

The first simple combination procedure aims to combine the  $\alpha_s(M_Z)$  central values and uncertainties obtained from the three classes of experiments analyzed in Sec. III.2, namely DIS, Jet+ $t\bar{t}$  combined, and DY. This procedure, is based on the  $\Delta\chi^2 = 1$  assumption and uses a criterion to inflate the resulting uncertainties suggested in the PDG [61]. The  $\alpha_s(M_Z)$  values corresponding to the minima of the individual  $\chi^2$  profiles are treated as independent determinations.<sup>7</sup> We further verify that the associated uncertainties are approximately Gaussian by fitting each  $\chi^2$  profile to a quadratic form, which results to be a valid assumption for the three classes of data we considered. This produces symmetric uncertainties, which represent a valid approximation in this specific case. The  $\alpha_s(M_Z)$  central values to be combined are summarized with their corresponding uncertainties  $\sigma_i$ , in Table IV.

	DIS	DY	Jet+ $t\bar{t}$	Combined
$\alpha_s(M_Z) \times 10^3$	115.14	118.62	120.65	<b>118.37</b>
Error ( $\sigma_i \times 10^3$ )	0.629	0.743	0.543	<b>0.360</b>

TABLE IV. Individual and combined determinations of  $\alpha_s(M_Z)$  from DIS, DY, and Jet+ $t\bar{t}$  data for the CT25prel baseline. Errors in the bottom row are obtained with  $\Delta\chi^2 = 1$ .

A combination of these determinations under the independence assumption requires the minimization of the following  $\chi^2_{\alpha_s}$  log-likelihood function:

$$\chi^2_{\alpha_s} = \sum_i \frac{(\alpha_s(M_Z) - \alpha_{s,i}(M_Z))^2}{\sigma_i^2} , \quad (6.1)$$

where  $\alpha_{s,i}$  and  $\sigma_i$  denote the central value and uncertainty for the  $i$ -th dataset listed in Table IV. The combined estimate and its variance are given by

$$\bar{\alpha}_s = \frac{\sum_i \alpha_{s,i}/\sigma_i^2}{\sum_i 1/\sigma_i^2} , \quad \sigma^2 = \frac{1}{\sum_i 1/\sigma_i^2} , \quad (6.2)$$

which result in  $\bar{\alpha}_s = 0.1184 \pm 0.0004$ , whose mean is consistent with the value obtained from the global  $\chi^2$  profile, thereby validating the underlying assumptions. However, the resulting uncertainty is significantly

<sup>7</sup> This assumption is strictly valid when each dataset is minimized independently. Although the profiles here are extracted from a global fit, we argue that this approximation is reasonable for the present analysis.

smaller than the uncertainties obtained in Sec. III.2 and than the current world average [61]. In addition, it produces  $\chi^2/\text{d.o.f.} \approx 22$ , indicating a dramatically bad quality of the fit. Therefore, this approach fails to capture the features of the various data in the baseline.

To improve on this, we apply the scale factor  $e_{S_{\text{PDG}}}$  as recommended by the PDG [61], that increases the uncertainties in such a way that the reduced  $\chi^2/\text{d.o.f.} \approx 1$ . This condition is guaranteed by choosing the scale factor as

$$e_{S_{\text{PDG}}} = \sqrt{\chi^2/\text{d.o.f.}} . \quad (6.3)$$

For the combination of values in Table IV, one finds  $e_{S_{\text{PDG}}} \approx \sqrt{22} \approx 4.7$ . In the context of one-dimensional data combination, this condition is equivalent to adopting a global tolerance of  $T \simeq 4.7$ . The application of the PDG rescaling results in

$$\alpha_s = 0.1184 \pm 0.0017 \quad (\text{scaled errors, } e_{S_{\text{PDG}}} \approx 4.7).$$

It is important to point out that such a rescaling procedure is not advised and is unsuitable in fits with poor quality. In such cases, an alternative, informed estimate of the uncertainty should be used. Motivated by this, we investigate other different approaches to estimate the  $\alpha_s(M_Z)$  uncertainty.

### VI.3. Final $\alpha_s$ determination

The four approaches that we choose for the final combination are based on the global and dynamical tolerances, as well as the two Bayesian models.

**Global and dynamical tolerances.** Sec. IV.1 described the commonly used uncertainty prescriptions based on the global and dynamical tolerance, or GT and DT. When we apply the GT criterion based on the 68% quantile for the sum of all  $\chi_E^2$  from the individual experiments, we obtain

$$\delta\alpha_s(M_Z) = 0.1184_{-0.0028}^{+0.0026} . \quad (6.4)$$

The DT procedure results in

$$\delta\alpha_s(M_Z) = 0.1184_{-0.0014}^{+0.0023}, \quad (6.5)$$

which exhibits substantial asymmetric uncertainty.

These results are obtained for the default pole mass  $m_c = 1.3$  GeV of the CT25 analysis. While in principle the charm mass is correlated with the gluon PDF and therefore  $\alpha_s$ , in practice this correlation is weak. Appendix B shows the GT and DT  $\alpha_s$  ranges for the alternative masses 1.2 and 1.4 GeV, and those

Statistical Method	Eq.	$\delta\alpha_s(M_Z)$
Global Tolerance	6.4	$0.1184^{+0.0026}_{-0.0028}$
Dynamical Tolerance	6.5	$0.1184^{+0.0024}_{-0.0012}$
BHM	5.3	$0.1181^{+0.0022}_{-0.0023}$
GMM	5.5	$0.1183^{+0.0023}_{-0.0023}$
Average		$0.1183^{+0.0023}_{-0.0020}$

TABLE V. Estimates of  $\alpha_s(M_Z)$  obtained by four distinct analyses of statistical uncertainty.

essentially coincide with the estimates for 1.3 GeV. The  $m_c$  dependence is hence found to be minimal, as is also illustrated by the  $\chi^2$  profiles in Fig. 15.

**Bayesian Models.** Section V deployed two Bayesian models to estimate  $\alpha_s$  uncertainties. We obtained  $\alpha_s(M_Z) = \alpha_s = 0.1181^{+0.0022}_{-0.0023}$  with the Bayesian Hierarchical Model and  $\alpha_s(M_Z) = 0.1183 \pm 0.0023$  with the Gaussian Mixture Model.

#### The average of four methods.

Table V collects the uncertainty estimates obtained with our four methods. The last row, labeled “Average”, corresponds to approximating the  $\alpha_s(M_Z)$  probability distribution from each statistical model as a split normal distribution and summing over each model with uniform weights to produce an average. This outcome average value and its uncertainty correspond to  $\alpha_s(M_Z) = 0.1183^{+0.0023}_{-0.0020}$ .

Good consistency among the four determinations increases our confidence in the result. It is important to emphasize that the determinations do not invoke a fixed tolerance value, or  $T^2$ . Instead, they would justify a specific  $T^2$ , should it be used as a proxy for the more complex approaches that we describe. For the CT25 baseline, the average  $\delta\alpha_s(M_Z)$  in Table V translates into the  $\Delta\chi^2 = +^{39}_{-25}$  for the global  $\chi^2$ . This is close, although not identical, to the approximate  $T^2 = 37$  at 68% CL introduced in the “CT two-tier tolerance” prescription used in the previous CT PDF analyses [16, 69, 80].

## VII. CONCLUSIONS

In this work, we presented a new determination of the strong coupling constant  $\alpha_s(M_Z)$  from the CT25 global QCD analysis at NNLO, incorporating high-precision LHC Run-2 data and improved methodologies. The final value of  $\alpha_s(M_Z)$  extracted from the CT25 global fit with its 68% CL uncertainty is

$$\alpha_s(M_Z) = 0.1183^{+0.0023}_{-0.0020}. \quad (7.1)$$

To assess in detail the variability of the central value and the  $\alpha_s(M_Z)$  uncertainty, we employed a suite of statistical models including global and dynamical tolerance criteria, Bayesian hierarchical models, and

Gaussian mixture models. We pointed out that this determination is nominal, and we identified several assumptions that may modify the outcome.

The key challenge for increasing the accuracy of the  $\alpha_s$  determination arises from insufficient information about the experimental correlated systematic errors that is made available to PDF fitters. In Sec. III.2, we investigated the sensitivity of  $\alpha_s(M_Z)$  to systematic uncertainty treatments in the data, particularly in inclusive-jet production, which shows significant variations in its preferences for the central value and uncertainty depending on the adapted treatment of its systematic errors. Two different choices for including the published systematic errors were considered: the multiplicative treatment normalizes the errors to the theory predictions; the additive treatment normalizes the error to the central value of the measurement. The multiplicative treatment produces results consistent with the world average, while applying the additive treatment across all jet measurements reveals substantial internal tensions among jet-production data sets. The actual nature of the correlated errors, which are likely to be neither fully multiplicative nor additive, may show deviations from these two scenarios. Experiments can reduce the associated uncontrolled ambiguity by publishing more complete models of their systematic uncertainties.

With the dynamic tolerance and cross-validation methods, the uncertainty estimates are sensitive to how the data is clustered. Section IV explored in detail the role of data clustering and random reshuffling of the residuals and nuisance parameters. We introduced a concept of data clustering safety that requires attention when tensions among data sets are present. The key idea is that the uncertainty on a fundamental parameter should not depend on how the individual data points are clustered, or at least the uncertainty associated with clustering must be estimated. Clustering safety is relevant both for the Hessian and Monte Carlo PDF methodologies and is more challenging when the experiments disagree.

In Sec. III.1, we also explored the impact of a large set of PDF parametrizations. In the case of the  $\alpha_s$  determination, the impact of the parametrization is small, as demonstrated by the tight clustering of best-fit values across roughly 287 alternative models in Fig. 1. These parametrizations have the functional form  $f(x, Q_0) = x^a(1 - x)^b P(x)$  where  $P(x)$  is an  $n$ -th order polynomial in  $x$  with  $2 \leq n \leq 5$ .

The impact of charm-quark mass variations was found to be minimal, with negligible shifts in the central value and uncertainty of  $\alpha_s(M_Z)$ .

Future experiments, seeking events coming from interactions beyond the standard model (BSM), will need to know trustworthy uncertainty ranges for the value of  $\alpha_s(M_Z) = \alpha_s(M_Z)^{(central)} \pm \delta\alpha_s$ .

## ACKNOWLEDGMENTS

The work of MG is partially supported by the National Science Foundation under Grants No. PHY-2412071. KM was supported in part by the US National Science Foundation under Grant PHY-2310497.

PMN and SD are grateful for support from the Wu-Ki Tung Endowed Chair in particle physics. The work of SD was also supported by the National Natural Science Foundation of China under Grant number 12475079. The work of CPY is supported by the U.S. National Science Foundation under Grants No. PHY-2310291.

### Appendix A: New LHC data sets included in the CT25 NNLO analysis

In this appendix, we provide additional details on the newly included data sets listed in Table I of the main narrative.

**Lepton pair production measurements.** As in the CT18A global fit, we include the precision measurement of  $W$  and  $Z$  production by ATLAS collaboration at 7 TeV [43]. This measurement revealed the enhancement in the strangeness PDF at  $x \sim 0.02$  – the trend that was corroborated by more recent LHC observations. In Ref. [40], we examined in depth the implications of these measurements for PDFs and identified the following differential cross sections for inclusion in the final CT25 fit:

1. From the ATLAS collaboration:
  - (a) muon pseudorapidity distribution in  $W$  boson production ( $W \rightarrow \mu\nu$ ) at a center-of-mass energy  $\sqrt{s} = 8$  TeV [26] with  $20.2 \text{ fb}^{-1}$  of integrated luminosity (IL), in the fiducial volume  $p_T^{l,\nu} > 25 \text{ GeV}$ ,  $|\eta_\mu| < 2.4$ ,  $m_T > 40 \text{ GeV}$ ;
  - (b)  $W^\pm$  muon pseudorapidity and  $Z$  dilepton rapidity distributions [29] at  $\sqrt{s} = 5.02$  TeV with  $25 \text{ pb}^{-1}$  of IL, in the fiducial phase space  $p_T^{l,\nu} > 25 \text{ GeV}$ ,  $|\eta_l| < 2.5$ ,  $m_T > 40 \text{ GeV}$  for  $W^\pm$  bosons, and  $p_T^l > 20 \text{ GeV}$ ,  $|\eta_l| < 2.5$ ,  $66 < m_{ll} < 116 \text{ GeV}$  for  $Z$  bosons;
  - (c) triple differential distribution in  $Z$  boson production in electron and muon decay channels [28], presented in terms of invariant mass  $m_{ll}$ , rapidity of dilepton pair  $y_{ll}$ , and cosine of the polar angle in the Collins-Soper frame, with an IL of  $35.9 \text{ fb}^{-1}$ ,  $p_T^l > 20 \text{ GeV}$ ,  $|\eta_l| < 2.4$ ,  $46 < m_{ll} < 200 \text{ GeV}$ .
2. From the CMS collaboration: rapidity distribution for the  $Z$  boson production at 13 TeV [27] with an IL of  $35.9 \text{ fb}^{-1}$ ,  $p_T^l > 20 \text{ GeV}$ ,  $|\eta_l| < 2.4$ , and  $|m_{ll} - M_Z| < 15 \text{ GeV}$ .
3. From the LHCb collaboration:
  - (a) electron pseudorapidity differential cross section in  $W \rightarrow e\nu$  production [30] at  $\sqrt{8}$  TeV with an IL of  $2 \text{ fb}^{-1}$ ,  $2.0 < \eta < 4.25$  and  $p_T^e > 20 \text{ GeV}$ ;

(b) dilepton rapidity distribution in  $Z$  boson production in electron and muon decay channels at  $\sqrt{s} = 13$  TeV [31] with  $0.29 \text{ fb}^{-1}$  of IL,  $2.0 < \eta_l < 4.5$ ,  $p_T^l > 20 \text{ GeV}$ ,  $60 < m_{ll} < 120 \text{ GeV}$ .

**Top-quark pair production measurements.** For top-quark pair production, we included the following measurements at  $\sqrt{s} = 13$  TeV based on the study of their impact on post-CT18 PDFs in Ref. [41]:

1. From the ATLAS collaboration:

- (a) rapidity distribution of the  $t\bar{t}$  pair,  $d\sigma/dy_{t\bar{t}}$ , in the all-hadronic channel [32] with an IL of  $36.1 \text{ fb}^{-1}$  in the full phase space at parton level;
- (b) the statistically combined  $m_{t\bar{t}} + y_{t\bar{t}} + y_{t\bar{t}}^B + H_T^{t\bar{t}}$  distributions [35], with  $36 \text{ fb}^{-1}$  of IL, where  $y_{t\bar{t}}^B$  denotes the reconstructed rapidity of the  $t\bar{t}$  system in the boosted topology, and  $H_T^{t\bar{t}}$  is the scalar sum of the transverse momenta of the hadronic and leptonic top quarks,  $H_T^{t\bar{t}} = p_t^{had} + p_t^{lep}$ .

2. From the CMS collaboration:

- (a) the  $y_{t\bar{t}}$  distribution in the dilepton channel [33] with  $35.9 \text{ fb}^{-1}$  of IL;
- (b) the  $m_{t\bar{t}}$  distribution in the lepton+jet channel [34] with  $137 \text{ fb}^{-1}$  of IL.

**Single-inclusive jet production measurements.** In Ref. [42], we compared constraints imposed on our post-CT18 PDFs by the latest LHC cross sections in hadronic jet production. While these cross sections can be included in the form of either inclusive single-jet or jet-pair distributions, Ref. [42] found it preferable to fit the single-inclusive jet cross sections only, in light of the stronger dependence of theory predictions in dijet production on the choice of renormalization and factorization scales. Based on the detailed examination of candidate jet cross sections in Ref. [42], the CT25 analysis includes the following single-inclusive jet production data sets:

1. From the ATLAS collaboration:

- (a) the  $d^2\sigma/(dp_T d|y|)$  distribution at  $\sqrt{s} = 8$  TeV [36] with  $20.2 \text{ fb}^{-1}$  of IL, jet radius  $R = 0.6$ , in the fiducial volume  $|y| < 3$  and  $70 \leq p_T^{jet} \leq 2500 \text{ GeV}$ ;
- (b) the  $d^2\sigma/(dp_T d|y|)$  distribution at  $\sqrt{s} = 13$  TeV [37] with  $3.2 \text{ fb}^{-1}$  of IL,  $R = 0.4$ ,  $|y| < 3$  and  $100 \leq p_T^{jet} \leq 3937 \text{ GeV}$ .

2. From the CMS collaboration, we include the  $d^2\sigma/dp_T d|y|$  distribution at  $\sqrt{s} = 13$  TeV [38] with  $33.5 \text{ fb}^{-1}$  of IL,  $R = 0.7$ ,  $|y| < 2$  and  $97 \leq p_T^{jet} \leq 3103 \text{ GeV}$ .

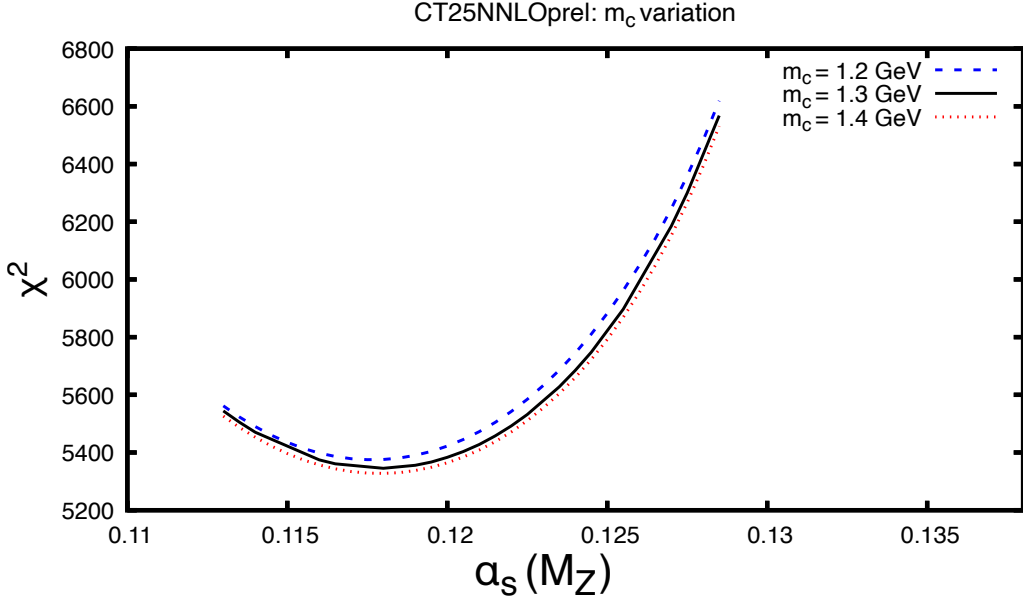


FIG. 15.  $\chi^2$  as a function of  $\alpha_s(M_Z)$  in correspondence of the three values of  $m_c$  considered in this analysis.

### Appendix B: Sensitivity to charm-quark mass variations

To investigate the sensitivity of the results to the charm-quark mass  $m_c$  (pole mass approximation), we extracted  $\alpha_s(M_Z)$  from two additional  $\chi^2_R$  scans obtained with  $m_c = 1.2$  GeV and  $m_c = 1.4$  GeV respectively. The default charm-quark mass value used in the CT25 global analysis is  $m_c = 1.3$  GeV.

From the global tolerance criterion, we obtain the following results with the CT25prel baseline:

$$\alpha_s(M_Z) = 0.1175_{-0.0023}^{+0.0025}, \quad m_c = 1.2 \text{ GeV}; \quad (\text{B1})$$

$$\alpha_s(M_Z) = 0.1179_{-0.0025}^{+0.0024}, \quad m_c = 1.3 \text{ GeV}; \quad (\text{B2})$$

$$\alpha_s(M_Z) = 0.1179_{-0.0025}^{+0.0024}, \quad m_c = 1.4 \text{ GeV}. \quad (\text{B3})$$

From this we note that the impact on the uncertainty is negligible, which is also reflected in Figure 15 showing the global  $\chi^2$  as a function of  $\alpha_s(M_Z)$  for the three values of  $m_c$ .

With the dynamical tolerance criterion we obtain at 68% CL:

$$\alpha_s(M_Z) = 0.1175_{-0.0011}^{+0.0019}, \quad m_c = 1.2 \text{ GeV}; \quad (\text{B4})$$

$$\alpha_s(M_Z) = 0.1179_{-0.0012}^{+0.0024}, \quad m_c = 1.3 \text{ GeV}; \quad (\text{B5})$$

$$\alpha_s(M_Z) = 0.1179_{-0.0013}^{+0.0025}, \quad m_c = 1.4 \text{ GeV}. \quad (\text{B6})$$

The DT errors from alternative clustering for the different  $m_c$  values behave similarly to those discussed in Sec. IV.

---

[1] D. d'Enterria *et al.*, *The strong coupling constant: state of the art and the decade ahead*, *J. Phys. G* **51**, 090501 (2024), [arXiv:2203.08271 \[hep-ph\]](https://arxiv.org/abs/2203.08271).

[2] G. P. Salam, The strong coupling: a theoretical perspective, in *From My Vast Repertoire ...: Guido Altarelli's Legacy*, edited by A. Levy, S. Forte, and G. Ridolfi (2019) pp. 101–121, [arXiv:1712.05165 \[hep-ph\]](https://arxiv.org/abs/1712.05165).

[3] F. Dulat, A. Lazopoulos, and B. Mistlberger, *iHixs 2 — Inclusive Higgs cross sections*, *Comput. Phys. Commun.* **233**, 243–260 (2018), [arXiv:1802.00827 \[hep-ph\]](https://arxiv.org/abs/1802.00827).

[4] S. Navas *et al.* (Particle Data Group Collaboration), *Review of particle physics*, *Phys. Rev. D* **110**, 030001 (2024).

[5] G. Aad *et al.* (ATLAS), *Determination of the strong coupling constant from transverse energy–energy correlations in multijet events at  $\sqrt{s} = 13$  TeV with the ATLAS detector*, *JHEP* **07**, 085, [arXiv:2301.09351 \[hep-ex\]](https://arxiv.org/abs/2301.09351).

[6] V. Chekhovsky *et al.* (CMS), *Determination of the strong coupling and its running from measurements of inclusive jet production*, *Phys. Lett. B* **868**, 139651 (2025), [arXiv:2412.16665 \[hep-ex\]](https://arxiv.org/abs/2412.16665).

[7] A. Hayrapetyan *et al.* (CMS), *Measurement of multijet azimuthal correlations and determination of the strong coupling in proton-proton collisions at  $\sqrt{s} = 13$  TeV*, *Eur. Phys. J. C* **84**, 842 (2024), [arXiv:2404.16082 \[hep-ex\]](https://arxiv.org/abs/2404.16082).

[8] A. Hayrapetyan *et al.* (CMS), *Measurement of Energy Correlators inside Jets and Determination of the Strong Coupling  $\alpha_S(m_Z)$* , *Phys. Rev. Lett.* **133**, 071903 (2024), [arXiv:2402.13864 \[hep-ex\]](https://arxiv.org/abs/2402.13864).

[9] G. Aad *et al.* (ATLAS), *A precise determination of the strong-coupling constant from the recoil of  $Z$  bosons with the ATLAS experiment at  $\sqrt{s} = 8$  TeV* (2023), [arXiv:2309.12986 \[hep-ex\]](https://arxiv.org/abs/2309.12986).

[10] V. Andreev *et al.* (H1), *Determination of the strong coupling constant  $\alpha_s(m_Z)$  in next-to-next-to-leading order QCD using H1 jet cross section measurements*, *Eur. Phys. J. C* **77**, 791 (2017), [Erratum: *Eur. Phys. J. C* 81, 738 (2021)], [arXiv:1709.07251 \[hep-ex\]](https://arxiv.org/abs/1709.07251).

[11] Y. Aoki *et al.* (Flavour Lattice Averaging Group (FLAG)), *FLAG Review 2024* (2024), [arXiv:2411.04268 \[hep-lat\]](https://arxiv.org/abs/2411.04268).

[12] National Academies of Sciences, Engineering, and Medicine, *Reproducibility and Replicability in Science* (The National Academies Press, Washington, DC, 2019).

[13] P. J. Mohr, D. B. Newell, B. N. Taylor, and E. Tiesinga, *Codata recommended values of the fundamental physical constants: 2022*, *Rev. Mod. Phys.* **97**, 025002 (2025).

[14] In preparation (2025).

[15] H.-L. Lai, J. Huston, Z. Li, P. Nadolsky, J. Pumplin, D. Stump, and C. P. Yuan, *Uncertainty induced by QCD coupling in the CTEQ global analysis of parton distributions*, *Phys. Rev. D* **82**, 054021 (2010), [arXiv:1004.4624 \[hep-ph\]](https://arxiv.org/abs/1004.4624).

[16] T.-J. Hou *et al.*, *New CTEQ global analysis of quantum chromodynamics with high-precision data from the LHC*, *Phys. Rev. D* **103**, 014013 (2021), [arXiv:1912.10053 \[hep-ph\]](https://arxiv.org/abs/1912.10053).

[17] S. Alekhin, J. Blümlein, S. Moch, and R. Placakyte, *Parton distribution functions,  $\alpha_s$ , and heavy-quark masses for LHC Run II*, *Phys. Rev. D* **96**, 014011 (2017), [arXiv:1701.05838 \[hep-ph\]](https://arxiv.org/abs/1701.05838).

[18] A. Gzhko *et al.*, *Running of the Charm-Quark Mass from HERA Deep-Inelastic Scattering Data*, *Phys. Lett.*

**B** **775**, 233–238 (2017), arXiv:1705.08863 [hep-ph].

[19] R. D. Ball, S. Carrazza, L. Del Debbio, S. Forte, Z. Kassabov, J. Rojo, E. Slade, and M. Ubiali (NNPDF), *Precision determination of the strong coupling constant within a global PDF analysis*, *Eur. Phys. J. C* **78**, 408 (2018), arXiv:1802.03398 [hep-ph].

[20] T. Cridge, L. A. Harland-Lang, A. D. Martin, and R. S. Thorne, *An investigation of the  $\alpha_S$  and heavy quark mass dependence in the MSHT20 global PDF analysis*, *Eur. Phys. J. C* **81**, 744 (2021), arXiv:2106.10289 [hep-ph].

[21] T. Cridge and M. A. Lim, *Constraining the top-quark mass within the global MSHT PDF fit*, *Eur. Phys. J. C* **83**, 805 (2023), arXiv:2306.14885 [hep-ph].

[22] S. Alekhin, M. V. Garzelli, S. O. Moch, and O. Zenaiev, *NNLO PDFs driven by top-quark data*, *Eur. Phys. J. C* **85**, 162 (2025), arXiv:2407.00545 [hep-ph].

[23] T. Cridge, L. A. Harland-Lang, and R. S. Thorne, *A first determination of the strong coupling  $\alpha_S$  at approximate  $N^3LO$  order in a global PDF fit*, *Eur. Phys. J. C* **84**, 1009 (2024), arXiv:2404.02964 [hep-ph].

[24] R. D. Ball, A. Barontini, J. Cruz-Martinez, S. Forte, F. Hekhorn, E. R. Nocera, J. Rojo, and R. Stegeman (NNPDF), *A Determination of  $\alpha_s(M_Z)$  at  $aN^3LO_{\text{QCD}} \otimes \text{NLO}_{\text{QED}}$  Accuracy from a Global PDF Analysis*, (2025), arXiv:2506.13871 [hep-ph].

[25] K. Kovařík, P. M. Nadolsky, and D. E. Soper, *Hadronic structure in high-energy collisions*, *Rev. Mod. Phys.* **92**, 045003 (2020), arXiv:1905.06957 [hep-ph].

[26] G. Aad *et al.* (ATLAS), *Measurement of the cross-section and charge asymmetry of  $W$  bosons produced in proton–proton collisions at  $\sqrt{s} = 8$  TeV with the ATLAS detector*, *Eur. Phys. J. C* **79**, 760 (2019), arXiv:1904.05631 [hep-ex].

[27] A. M. Sirunyan *et al.* (CMS), *Measurements of differential  $Z$  boson production cross sections in proton-proton collisions at  $\sqrt{s} = 13$  TeV*, *JHEP* **12**, 061, arXiv:1909.04133 [hep-ex].

[28] M. Aaboud *et al.* (ATLAS), *Measurement of the Drell-Yan triple-differential cross section in  $pp$  collisions at  $\sqrt{s} = 8$  TeV*, *JHEP* **12**, 059, arXiv:1710.05167 [hep-ex].

[29] M. Aaboud *et al.* (ATLAS), *Measurements of  $W$  and  $Z$  boson production in  $pp$  collisions at  $\sqrt{s} = 5.02$  TeV with the ATLAS detector*, *Eur. Phys. J. C* **79**, 128 (2019), [Erratum: Eur.Phys.J.C 79, 374 (2019)], arXiv:1810.08424 [hep-ex].

[30] R. Aaij *et al.* (LHCb), *Measurement of forward  $W \rightarrow e\nu$  production in  $pp$  collisions at  $\sqrt{s} = 8$  TeV*, *JHEP* **10**, 030, arXiv:1608.01484 [hep-ex].

[31] R. Aaij *et al.* (LHCb), *Precision measurement of forward  $Z$  boson production in proton-proton collisions at  $\sqrt{s} = 13$  TeV*, *JHEP* **07**, 026, arXiv:2112.07458 [hep-ex].

[32] G. Aad *et al.* (ATLAS), *Measurements of top-quark pair single- and double-differential cross-sections in the all-hadronic channel in  $pp$  collisions at  $\sqrt{s} = 13$  TeV using the ATLAS detector*, *JHEP* **01**, 033, arXiv:2006.09274 [hep-ex].

[33] A. M. Sirunyan *et al.* (CMS), *Measurements of  $t\bar{t}$  differential cross sections in proton-proton collisions at  $\sqrt{s} = 13$  TeV using events containing two leptons*, *JHEP* **02**, 149, arXiv:1811.06625 [hep-ex].

[34] A. Tumasyan *et al.* (CMS), *Measurement of differential  $t\bar{t}$  production cross sections in the full kinematic range*

using lepton+jets events from proton-proton collisions at  $\sqrt{s} = 13$  TeV, *Phys. Rev. D* **104**, 092013 (2021), arXiv:2108.02803 [hep-ex].

[35] G. Aad *et al.* (ATLAS), Measurements of top-quark pair differential and double-differential cross-sections in the  $\ell+jets$  channel with  $pp$  collisions at  $\sqrt{s} = 13$  TeV using the ATLAS detector, *Eur. Phys. J. C* **79**, 1028 (2019), [Erratum: Eur.Phys.J.C 80, 1092 (2020)], arXiv:1908.07305 [hep-ex].

[36] M. Aaboud *et al.* (ATLAS), Measurement of the inclusive jet cross-sections in proton-proton collisions at  $\sqrt{s} = 8$  TeV with the ATLAS detector, *JHEP* **09**, 020, arXiv:1706.03192 [hep-ex].

[37] M. Aaboud *et al.* (ATLAS), Measurement of inclusive jet and dijet cross-sections in proton-proton collisions at  $\sqrt{s} = 13$  TeV with the ATLAS detector, *JHEP* **05**, 195, arXiv:1711.02692 [hep-ex].

[38] V. Khachatryan *et al.* (CMS), Measurement and QCD analysis of double-differential inclusive jet cross sections in  $pp$  collisions at  $\sqrt{s} = 8$  TeV and cross section ratios to 2.76 and 7 TeV, *JHEP* **03**, 156, arXiv:1609.05331 [hep-ex].

[39] H.-L. Lai, M. Guzzi, J. Huston, Z. Li, P. M. Nadolsky, J. Pumplin, and C. P. Yuan, New parton distributions for collider physics, *Phys. Rev. D* **82**, 074024 (2010), arXiv:1007.2241 [hep-ph].

[40] I. Sitiwaldi, K. Xie, A. Ablat, S. Dulat, T.-J. Hou, and C. . P. Yuan (CTEQ-TEA), Precision studies of the post-CT18 LHC Drell-Yan data in the CTEQ-TEA global analysis, *Phys. Rev. D* **108**, 034030 (2023), arXiv:2305.10733 [hep-ph].

[41] A. Ablat, M. Guzzi, K. Xie, S. Dulat, T.-J. Hou, I. Sitiwaldi, and C. P. Yuan, Exploring the impact of high-precision top-quark pair production data on the structure of the proton at the LHC, *Phys. Rev. D* **109**, 054027 (2024), arXiv:2307.11153 [hep-ph].

[42] A. Ablat, S. Dulat, T.-J. Hou, J. Huston, P. Nadolsky, I. Sitiwaldi, K. Xie, and C. P. Yuan (CTEQ-TEA), Impact of LHC precision measurements of inclusive jet and dijet production on the CTEQ-TEA global PDF fit, *Phys. Rev. D* **111**, 036033 (2025), arXiv:2412.00350 [hep-ph].

[43] M. Aaboud *et al.* (ATLAS), Precision measurement and interpretation of inclusive  $W^+$ ,  $W^-$  and  $Z/\gamma^*$  production cross sections with the ATLAS detector, *Eur. Phys. J. C* **77**, 367 (2017), arXiv:1612.03016 [hep-ex].

[44] H. Abramowicz *et al.* (ZEUS, H1), Combination and QCD Analysis of Charm Production Cross Section Measurements in Deep-Inelastic ep Scattering at HERA, *Eur. Phys. J. C* **73**, 2311 (2013), arXiv:1211.1182 [hep-ex].

[45] A. Aktas *et al.* (H1), Measurement of  $F2(c\bar{c})$  and  $F2(b\bar{b})$  at high  $Q^2$  using the H1 vertex detector at HERA, *Eur. Phys. J. C* **40**, 349–359 (2005), arXiv:hep-ex/0411046 [hep-ex].

[46] H. Abramowicz *et al.* (H1, ZEUS), Combination and QCD analysis of charm and beauty production cross-section measurements in deep inelastic ep scattering at HERA, *Eur. Phys. J. C* **78**, 473 (2018), arXiv:1804.01019 [hep-ex].

[47] J. Dove *et al.* (SeaQuest), The asymmetry of antimatter in the proton, *Nature* **590**, 561–565 (2021), [Erratum: Nature 604, E26 (2022)], arXiv:2103.04024 [hep-ph].

[48] J. P. Berge *et al.*, A Measurement of Differential Cross-Sections and Nucleon Structure Functions in Charged Current Neutrino Interactions on Iron, *Z. Phys. C* **49**, 187–224 (1991).

[49] U.-K. Yang *et al.* (CCFR/NuTeV), Measurements of  $F_2$  and  $xF_3^\nu - xF_3^{\bar{\nu}}$  from CCFR  $\nu_\mu$ -Fe and  $\bar{\nu}_\mu$ -Fe data

in a physics model independent way, *Phys. Rev. Lett.* **86**, 2742–2745 (2001), arXiv:hep-ex/0009041 [hep-ex].

[50] W. G. Seligman *et al.*, Improved determination of  $\alpha(s)$  from neutrino nucleon scattering, *Phys. Rev. Lett.* **79**, 1213–1216 (1997), arXiv:hep-ex/9701017 [hep-ex].

[51] E. Rondio (NMC), Nuclear effects in deep inelastic scattering, *Nucl. Phys. A* **553**, 615C–624C (1993).

[52] F. D. Aaron *et al.* (H1), Measurement of the Inclusive  $e \backslash p_{\text{mp}}$  Scattering Cross Section at High Inelasticity  $y$  and of the Structure Function  $F_L$ , *Eur. Phys. J. C* **71**, 1579 (2011), arXiv:1012.4355 [hep-ex].

[53] W. Seligman, Ph.D. thesis, Columbia U. (1997).

[54] U.-K. Yang *et al.* (CCFR/NuTeV), A Measurement of  $R = \sigma_L / \sigma_T$  in deep inelastic neutrino - nucleon scattering at the Tevatron, *J. Phys. G* **22**, 775–780 (1996), arXiv:hep-ex/9605005.

[55] J. Pumplin, D. R. Stump, J. Huston, H. L. Lai, P. M. Nadolsky, and W.-K. Tung, New generation of parton distributions with uncertainties from global QCD analysis, *JHEP* **07**, 012, arXiv:hep-ph/0201195 [hep-ph].

[56] J. Gao, M. Guzzi, and P. M. Nadolsky, Charm quark mass dependence in a global QCD analysis, *Eur. Phys. J. C* **73**, 2541 (2013), arXiv:1304.3494 [hep-ph].

[57] R. D. Ball *et al.*, Parton Distribution Benchmarking with LHC Data, *JHEP* **04**, 125, arXiv:1211.5142 [hep-ph].

[58] S. Forte and Z. Kassabov, Why  $\alpha_s$  cannot be determined from hadronic processes without simultaneously determining the parton distributions, *Eur. Phys. J. C* **80**, 182 (2020), arXiv:2001.04986 [hep-ph].

[59] S. Forte, J. Rojo, and R. Stegeman, in *2025 European Physical Society Conference on High Energy Physics* (2025) arXiv:2511.22561 [hep-ph].

[60] P. Bevington and D. K. Robinson, *Data Reduction and Error Analysis for the Physical Sciences* (McGraw-Hill Education, 2002).

[61] S. Navas *et al.* (Particle Data Group), Review of particle physics, *Phys. Rev. D* **110**, 030001 (2024).

[62] P. Jimenez-Delgado and E. Reya, Delineating parton distributions and the strong coupling, *Phys. Rev. D* **89**, 074049 (2014), arXiv:1403.1852 [hep-ph].

[63] S. Alekhin, J. Blümlein, and S. Moch, NLO PDFs from the ABMP16 fit, *Eur. Phys. J. C* **78**, 477 (2018), arXiv:1803.07537 [hep-ph].

[64] I. Abt *et al.* (H1, ZEUS), Impact of jet-production data on the next-to-next-to-leading-order determination of HERAPDF2.0 parton distributions, *Eur. Phys. J. C* **82**, 243 (2022), arXiv:2112.01120 [hep-ex].

[65] G. D'Agostini, On the use of the covariance matrix to fit correlated data, *Nucl. Instrum. Meth. A* **346**, 306–311 (1994).

[66] G. D'Agostini, *Bayesian reasoning in high-energy physics: Principles and applications* (1999).

[67] R. D. Ball, L. Del Debbio, S. Forte, A. Guffanti, J. I. Latorre, J. Rojo, and M. Ubiali (NNPDF), Fitting Parton Distribution Data with Multiplicative Normalization Uncertainties, *JHEP* **05**, 075, arXiv:0912.2276 [hep-ph].

[68] J. Pumplin, D. Stump, R. Brock, D. Casey, J. Huston, J. Kalk, H.-L. Lai, and W.-K. Tung, Uncertainties of predictions from parton distribution functions. 2. The Hessian method, *Phys. Rev. D* **65**, 014013 (2001), arXiv:hep-ph/0101032 [hep-ph].

[69] J. Gao, M. Guzzi, J. Huston, H.-L. Lai, Z. Li, P. Nadolsky, J. Pumplin, D. Stump, and C. P. Yuan, CT10 next-to-next-to-leading order global analysis of QCD, *Phys. Rev. D* **89**, 033009 (2014), arXiv:1302.6246 [hep-ph].

- [70] A. D. Martin, W. J. Stirling, R. S. Thorne, and G. Watt, *Parton distributions for the LHC*, *Eur. Phys. J. C* **63**, 189–285 (2009), arXiv:0901.0002 [hep-ph].
- [71] R. A. Fisher, *Statistical methods for research workers* (Oliver and Boyd, Edinburgh, 1925) Chap. 4, an Internet version of the 1st edition at <http://psychclassics.yorku.ca/Fisher/Methods/>.
- [72] T. Lewis, *A simple improved-accuracy normal approximation for  $\chi^2$* , *Australian Journal of Statistics* **30A**, 160–168 (1988).
- [73] M. Matsumoto and T. Nishimura, *Mersenne twister: a 623-dimensionally equidistributed uniform pseudo-random number generator*, *ACM Transactions on Modeling and Computer Simulation* **8**, 3–30 (1998).
- [74] R. D. Ball *et al.* (NNPDF), *The path to proton structure at 1% accuracy*, *Eur. Phys. J. C* **82**, 428 (2022), arXiv:2109.02653 [hep-ph].
- [75] S. Forte and S. Carrazza, *Parton distribution functions*, Artificial Intelligence for Particle Physics **World Scientific Publishing** (2020), arXiv:2008.12305 [hep-ph].
- [76] J. Erler and R. Ferro-Hernández, *Alternative to the application of PDG scale factors*, *Eur. Phys. J. C* **80**, 541 (2020), arXiv:2004.01219 [physics.data-an].
- [77] M. Yan, T.-J. Hou, Z. Li, K. Mohan, and C. P. Yuan, *Generalized statistical model for fits to parton distributions*, *Phys. Rev. D* **112**, 034008 (2025), arXiv:2406.01664 [hep-ph].
- [78] H. Akaike, *A new look at the statistical model identification*, *IEEE Transactions on Automatic Control* **19**, 716–723 (1974).
- [79] G. Schwarz, *Estimating the Dimension of a Model*, *The Annals of Statistics* **6**, 461 – 464 (1978).
- [80] S. Dulat, T.-J. Hou, J. Gao, M. Guzzi, J. Huston, P. Nadolsky, J. Pumplin, C. Schmidt, D. Stump, and C.-P. Yuan, *New parton distribution functions from a global analysis of quantum chromodynamics*, *Phys. Rev. D* **93**, 033006 (2016), arXiv:1506.07443 [hep-ph].